Antarctic Science page 1 of 24 *(2024)* doi:10.1017/S0954102023000287

Geological insights from the newly discovered granite of Sif Island between Thwaites and Pine Island glaciers

JAMES W. MARSCHALEK [1], STUART N. THOMSON [2], CLAUS-DIETER HILLENBRAND [3], PIETER VERMEESCH [4], CHRISTINE SIDDOWAY [5], ANDREW CARTER [6], KEIR NICHOLS [1], DYLAN H. ROOD [1], RYAN A. VENTURELLI [7], SAMANTHA J. HAMMOND [8], JULIA WELLNER [9] and TINA VAN DE FLIERDT [1]

[1]*Department of Earth Science and Engineering, Imperial College London, Exhibition Road, London, SW7 2BP, UK*
[2]*Department of Geosciences, University of Arizona, 1040 E. 4th Street, Tucson, AZ 85721, USA*
[3]*British Antarctic Survey, High Cross, Madingley Road, Cambridge, CB3 0ET, UK*
[4]*Department of Earth Sciences, University College London, London, WC1E 6BT, UK*
[5]*Department of Geology, The Colorado College, Colorado Springs, CO 80903, USA*
[6]*Department of Earth and Planetary Sciences, Birkbeck, University of London, London, WC1E 7HX, UK*
[7]*Department of Geology and Geological Engineering, Colorado School of Mines, Golden, CO 80401, USA*
[8]*School of Environment, Earth and Ecosystem Sciences, The Open University, Milton Keynes, MK7 6AA, UK*
[9]*Department of Earth and Atmospheric Sciences, University of Houston, Houston, TX 77004, USA*
jwm17@ic.ac.uk

Abstract: Large-scale geological structures have controlled the long-term development of the bed and thus the flow of the West Antarctic Ice Sheet (WAIS). However, complete ice cover has obscured the age and exact positions of faults and geological boundaries beneath Thwaites Glacier and Pine Island Glacier, two major WAIS outlets in the Amundsen Sea sector. Here, we characterize the only rock outcrop between these two glaciers, which was exposed by the retreat of slow-flowing coastal ice in the early 2010s to form the new Sif Island. The island comprises granite, zircon U-Pb dated to ~177–174 Ma and characterized by initial ε_{Nd}, $^{87}Sr/^{86}Sr$ and ε_{Hf} isotope compositions of -2.3, 0.7061 and -1.3, respectively. These characteristics resemble Thurston Island/Antarctic Peninsula crustal block rocks, strongly suggesting that the Sif Island granite belongs to this province and placing the crustal block's boundary with the Marie Byrd Land province under Thwaites Glacier or its eastern shear margin. Low-temperature thermochronological data reveal that the granite underwent rapid cooling following emplacement, rapidly cooled again at ~100–90 Ma and then remained close to the Earth's surface until present. These data help date vertical displacement across the major tectonic structure beneath Pine Island Glacier to the Late Cretaceous.

Received 7 April 2023, accepted 4 September 2023

Key words: Geochemistry, Pine Island Bay, thermochronology, West Antarctica, zircon Hf isotopes, zircon U-Pb geochronology

Introduction

The exposure of new islands in polar regions is a visually powerful symptom of a warming climate. These islands are appearing due to the retreat of ice caps and ice sheets, compounded by local sea-level fall caused by isostatic uplift of surrounding coastal areas and/or reduction in gravitational 'pull' on the ocean by the waning ice sheet (e.g. Ziaja & Ostafi 2019, Hansen *et al.* 2022). In 2020, a hitherto uncharted small island, informally named Sif Island, was discovered during expedition NBP20-02 of RV/IB *Nathaniel B. Palmer*, part of the Thwaites Offshore Research (THOR) project (see https://thwaitesglacieroffshoreresearch.org/). Sif Island is located in Pine Island Bay of the eastern Amundsen Sea Embayment (latitude: -75°05'42", longitude: -102°49'30"; Fig. 1). Subsequent analysis of satellite imagery revealed that Sif Island became isolated from the main West Antarctic Ice Sheet (WAIS) by a decade of retreat of slow-flowing ice between Thwaites Glacier and Pine Island Glacier (Fig. 2).

The newly exposed granitic rock at Sif Island is uniquely situated to address unresolved tectonic and glaciological hypotheses that hinder progress towards a better understanding of the ice-bed interaction, and thus flow dynamics, of Thwaites and Pine Island glaciers. Together, these two glaciers drain approximately a third of the largely marine-based and inherently unstable

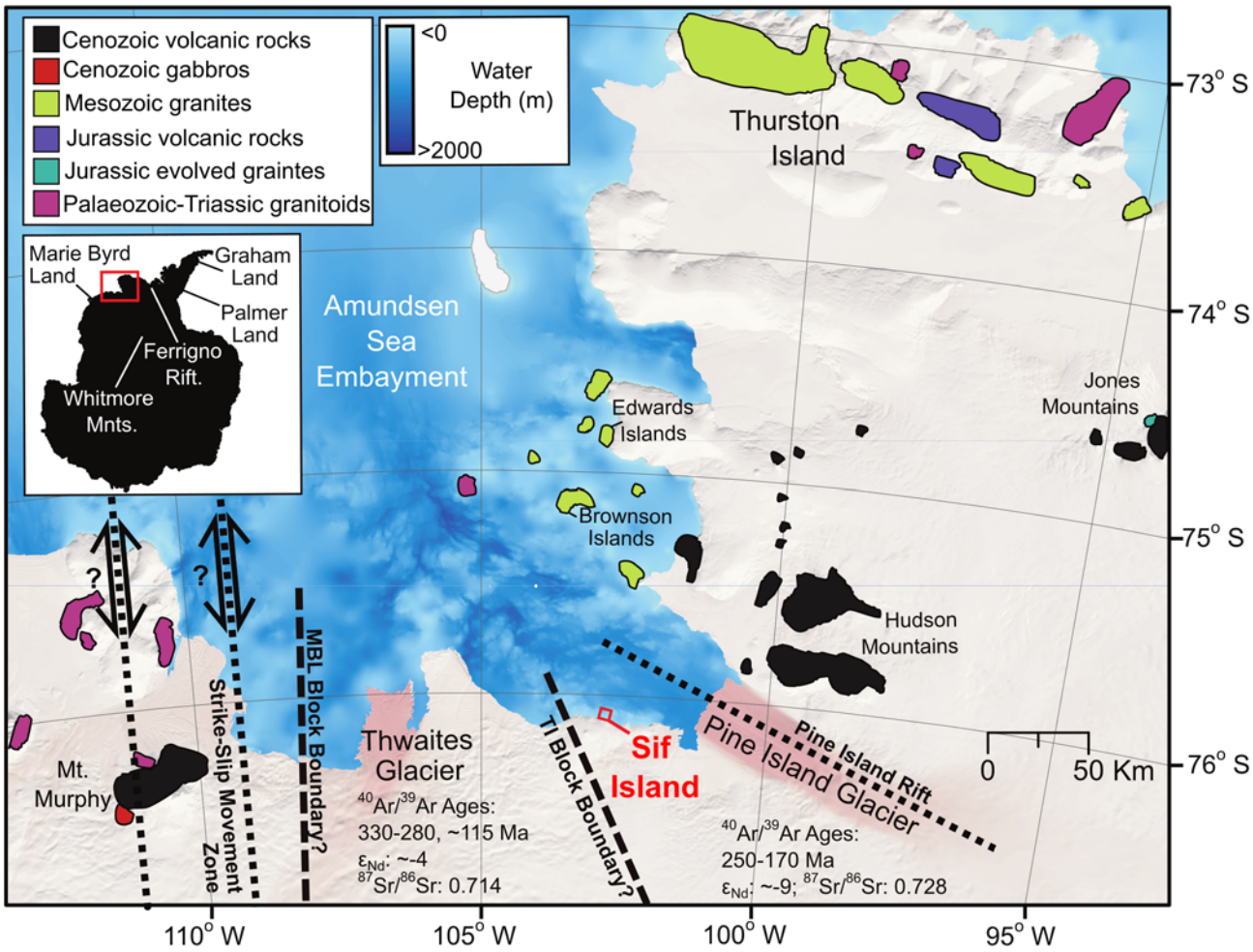

Figure 1. Location of Sif Island in the eastern Amundsen Sea Embayment relative to other rock exposures, which are mapped based on Cox *et al.* (2019) and classified based on Simões Pereira *et al.* (2020). The location of the main map within Antarctica is shown in the top-left insert (red box), and the position of Sif Island (corresponding to Fig. 2) is indicated in the main map (red box). The approximate position of Pine Island Rift is from Jordan *et al.* (2010) and the position of the strike-slip movement zone near Mount Murphy is from Spiegel *et al.* (2016), although the sense of the fault motion is indicated as uncertain due to disagreement with Müller *et al.* (2007). The uncertain Thurston Island (TI) and Marie Byrd Land (MBL) crustal block boundaries are displayed following Zundel *et al.* (2019b). Hornblende and biotite $^{40}Ar/^{39}Ar$ age populations, ε_{Nd} values and $^{87}Sr/^{86}Sr$ data for detritus shed from Pine Island and Thwaites glaciers are from Simões Pereira *et al.* (2020). Offshore bathymetry is from Hogan *et al.* (2020), with *BedMachine Antarctica* v.1 (Morlighem *et al.* 2020) used where these data were absent. Ice-sheet extent data are from the Scientific Committee on Antarctic Research (SCAR) Antarctic Digital Database, accessed 2022 (Gerrish *et al.* 2022). On the ice, MODIS ice imagery is displayed (Haran *et al.* 2014), and red shading indicates faster ice-flow velocities (Mouginot *et al.* 2019), where Thwaites and Pine Island glaciers are located.

WAIS into the Amundsen Sea Embayment (Rignot *et al.* 2019), with an ice volume sufficient to raise sea level by ~1.2 m (Morlighem *et al.* 2020). As these glaciers comprise one of the most sensitive parts of the Antarctic cryosphere, understanding them is critical for predicting the magnitude and rate of future global sea-level rise from WAIS loss (Scambos *et al.* 2017, Intergovernmental Panel on Climate Change 2019).

Underlying geological features and boundaries influence the flow of overlying ice and fundamentally shape ice drainage patterns in the Amundsen Sea sector of the WAIS. Sif Island is the only rock exposure between Pine Island and Thwaites glaciers. Characterizing the petrology and geochemistry of Sif Islands granitic bedrock is therefore essential to refine the geological and tectonic framework of the Amundsen Sea Embayment and affirm the origins of large-scale features of the modern seabed extending beneath the ice. Additionally, measurements of cosmogenic nuclides can help determine the exposure history of the island and place the observed recent ice-sheet margin retreat in a long-term context.

https://doi.org/10.1017/S0954102023000287 Published online by Cambridge University Press

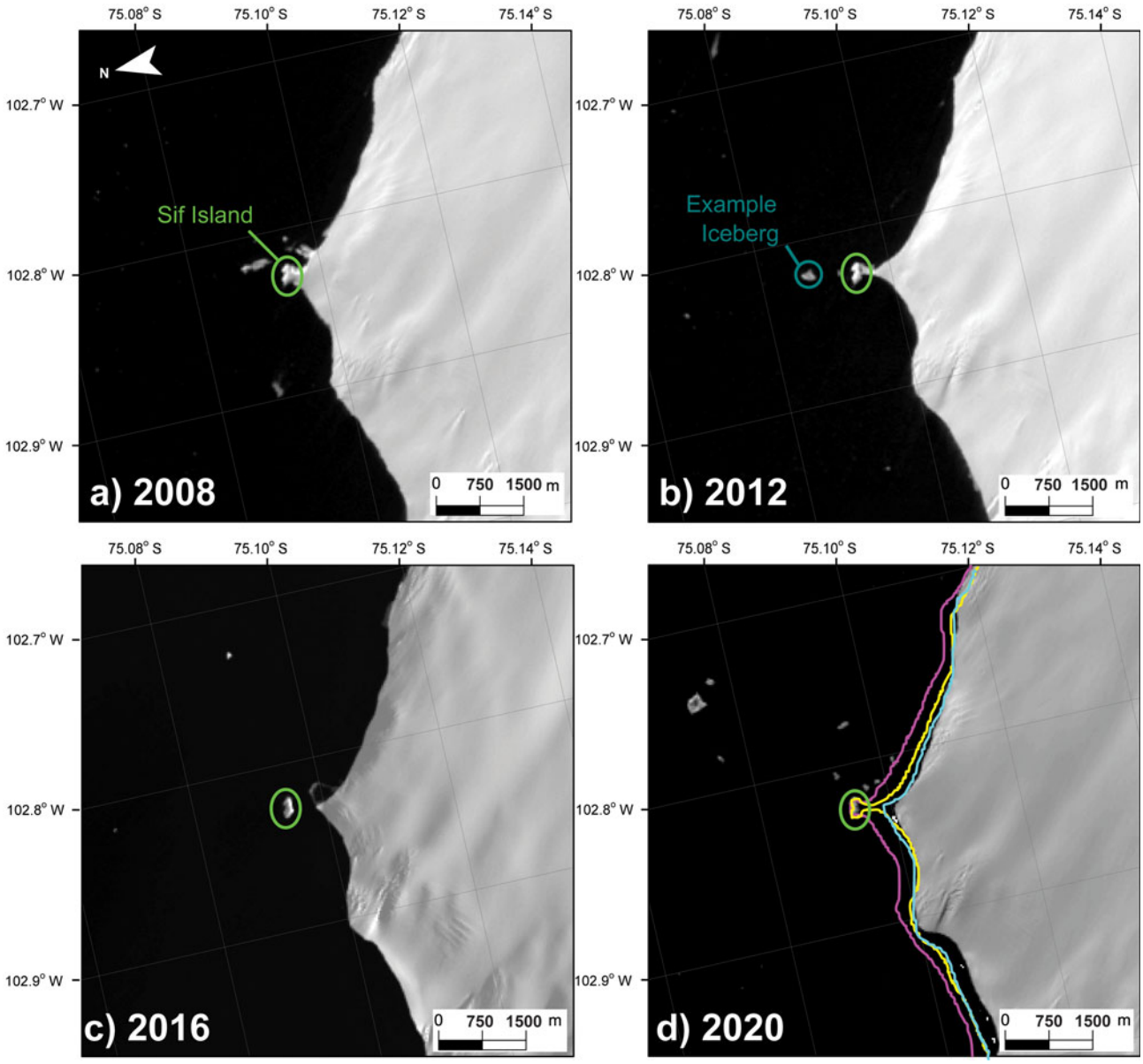

Figure 2. The exposure of Sif Island caused by a retreating ice front captured in LANDSAT imagery from 23 November 2008 (**a.** Landsat 7), 18 November 2012 (**b.** Landsat 7), 11 January 2016 (**c.** Landsat 8) and 26 January 2020 (**d.** Landsat 8). Landsat Operational Land Imager/Thermal Infrared Sensor (OLI/TIRS) imagery courtesy of the United States Geological Survey. The ice margin retreated by ~500 m in the 12 year period. Panel **d.** shows previous ice extents in **a.**–**c.** as magenta, yellow and cyan lines, respectively. The position of Sif Island is circled in green, with an example iceberg circled in teal in panel **b.** for comparison. The location of the map within Pine Island Bay is shown in Fig. 1.

Geological setting

The Amundsen Sea Embayment coincides with a lithospheric boundary between the crustal blocks of Thurston Island and Marie Byrd Land in West Antarctica (Fig. 1; e.g. Jordan *et al.* 2020). Deep bed topography and bedrock lineaments imply the localization of the WAIS outlet glaciers/ice streams along fault zones. For example, Pine Island Rift lies beneath Pine Island Glacier (Jordan *et al.* 2010, Gohl 2012), and a wrench system bordering Mount Murphy lies on the western side of Thwaites Glacier (Spiegel *et al.* 2016). Sif Island is located on the southern margin of Pine Island Bay (Fig. 1). Despite diverse geophysical data obtained from gravimetric, magnetic, bathymetric and seismic surveys of the region (e.g. Diehl *et al.* 2008, Jordan *et al.* 2010, Kalberg *et al.* 2015), consensus has not been reached regarding the specific position of the tectonic boundary between the Marie Byrd Land and Thurston Island crustal blocks (Fig. 1). Some workers

https://doi.org/10.1017/S0954102023000287 Published online by Cambridge University Press

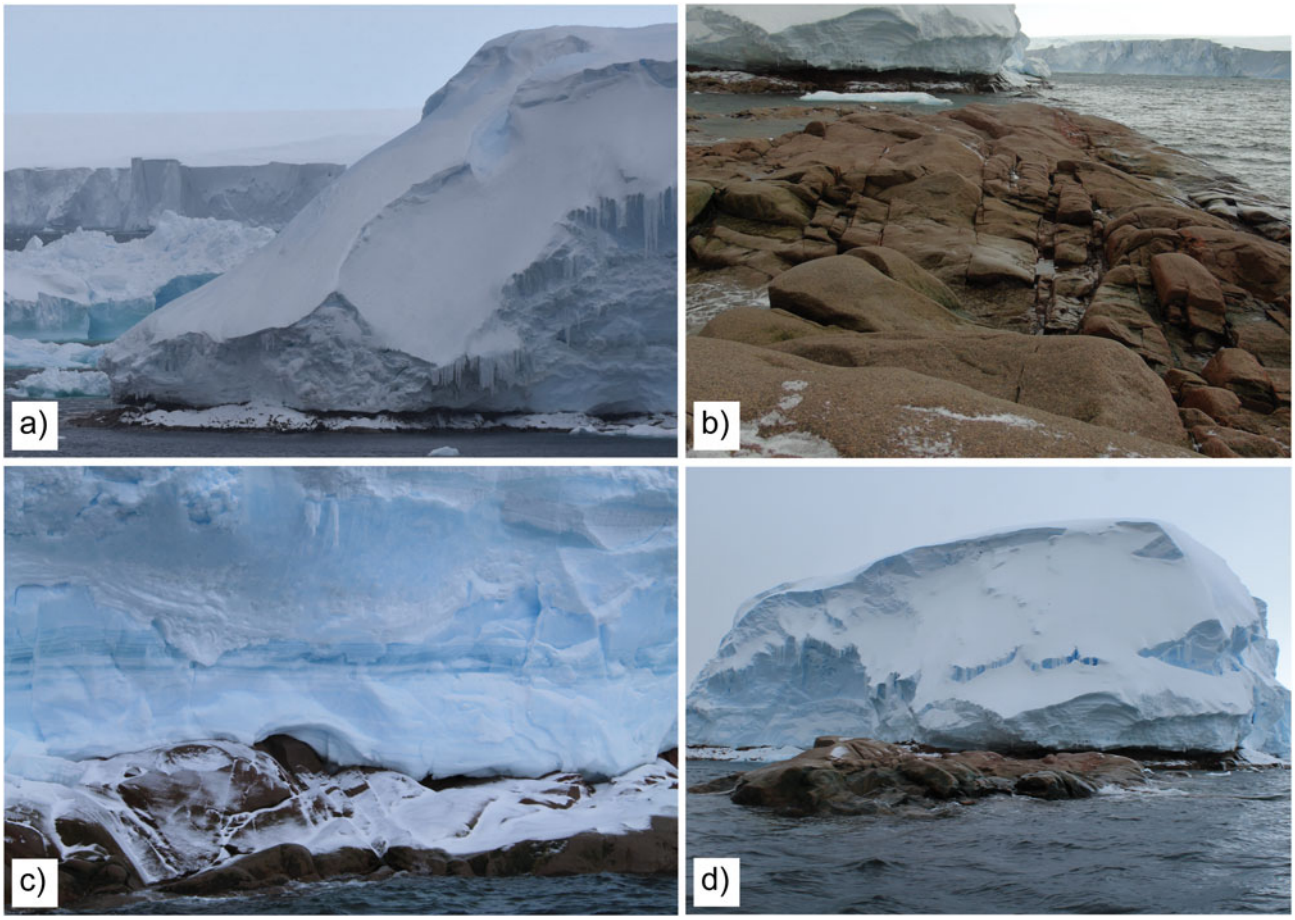

Figure 3. Field photographs of Sif Island. **a.** The ~40–50 m-thick ice cover of the island (right), remaining after retreat of the West Antarctic Ice Sheet margin, which is visible in the background. Grounded icebergs are present between the modern ice-sheet margin and the island (left). **b.** Exposed rock on the promontory (i.e. sampling location), with the main island visible in the top-left of the image. Exposed rock is ~5 m × ~20 m. **c.** A typical section of the basal ice and rock exposure. Melt layers are visible in the ice, and the height of the exposed rock between the water line and ice cover is ~1–2 m. **d.** Promontory rising ~1 m above sea level, with the main island in the background.

portray the Thurston Island crustal block boundary along Pine Island Rift (e.g. Gohl *et al.* 2007, Dunham *et al.* 2020, Jordan *et al.* 2020), whereas others project it beneath Thwaites Glacier (e.g. Kalberg *et al.* 2015, Spiegel *et al.* 2016, Zundel *et al.* 2019b). The kinematics of parallel structures within the boundary zone have been determined using diverse criteria and are also uncertain. Spiegel *et al.* (2016) interpreted sinistral transtension along the Mount Murphy wrench system based on bedrock thermochronology and structural geometries. In contrast, Müller *et al.* (2007) determined a dextral sense for the Ferrigno Rift, on the eastern margin of the Thurston Island block, using plate motions during the Cenozoic opening of the West Antarctic Rift System.

A further debate resulting from a dearth of bedrock exposure is whether Cenozoic structures reactivate faults that formed during Mesozoic tectonism across West Antarctica (e.g. Kalberg *et al.* 2015, Dziadek *et al.* 2021). In the Amundsen Sea Embayment and its WAIS drainage sector, the prominent crustal structures controlling the bathymetry/bed topography and lithospheric boundaries formed during the Cenozoic phase of deformation in this part of the West Antarctic Rift System (Müller *et al.* 2007, Dziadek *et al.* 2021), with Pine Island Rift having been active during the early Cenozoic (Jordan *et al.* 2010, Gohl *et al.* 2013, Spiegel *et al.* 2016). However, it is unclear whether Pine Island Rift exploited a pre-existing structure or whether it formed across the crust of the Thurston Island block. Characterizing the age, origin and thermal history of the Sif Island granite will inform this debate, as well as helping constrain the location of the Marie Byrd Land-Thurston Island block boundaries.

Exposed rocks elsewhere around the Amundsen Sea Embayment show that both Marie Byrd Land and

https://doi.org/10.1017/S0954102023000287 Published online by Cambridge University Press

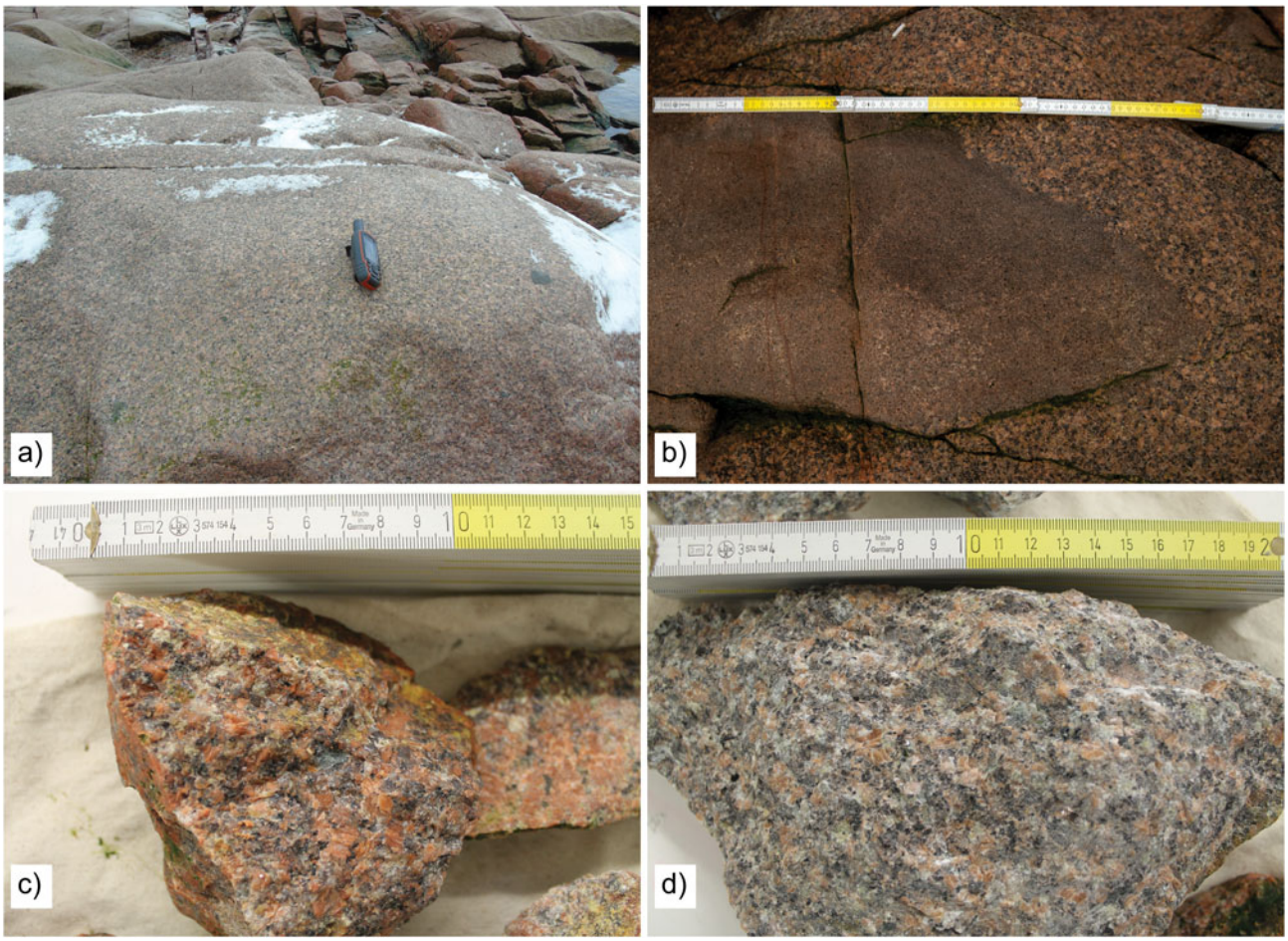

Figure 4. Photographs of the Sif Island rock exposure. **a.** Typical exposed bedrock surface with GPS handset for scale. **b.** Contact between a coarse-grained granite forming the bulk of the outcrop and a finer-grained enclave. **c.** Hand specimen of a 'pinker' sample (e.g. SIA and SIC; SI = Sif Island). **d.** Hand specimen of sample SIB, collected just below the exposure shown in panel **a**. Each yellow and white section on the folding rule is 10 cm.

Thurston Island contain plutonic rocks formed in a convergent plate boundary setting since the mid-Palaeozoic (Pankhurst *et al.* 1998, Riley *et al.* 2017). The two tectonic provinces differ as Marie Byrd Land is underlain by Proterozoic lithosphere and contains exposures of Cretaceous migmatite, whereas Thurston Island contains Jurassic evolved granites and volcanics (e.g. Jordan *et al.* 2020). Neogene volcanic rocks are present in the Hudson Mountains, north of the Pine Island Glacier terminus, and as isolated volcanoes, such as Mount Murphy, to the west of Thwaites Glacier (Fig. 1). Distributed volcanic centres are larger and more numerous across the Marie Byrd Land province (Wilch *et al.* 2021), and Neogene volcanic rocks probably continue beneath the WAIS, inferred from magnetic anomalies, radar data and geochemical data (e.g. Behrendt 2013, van Wyk de Vries *et al.* 2017, Simões Pereira *et al.* 2020). Cretaceous to Cenozoic sedimentary strata underlie parts of the drainage basins of both glaciers as well as the continental shelf (Smith *et al.* 2013, Schroeder *et al.* 2014, Muto *et al.* 2019, Klages *et al.* 2020, Simões Pereira *et al.* 2020).

Field observations

Sampling of Sif Island was conducted opportunistically on behalf of the THOR project during expedition NBP20-02 with RV/IB *Nathaniel B. Palmer* in early 2020. The island was named after the Norse goddess Sif, the wife of Thor, in association with the THOR project. THOR is part of the wider International Thwaites Glacier Collaboration (ITGC) programme, a joint US (National Science Foundation) and UK (Natural Environment Research Council) initiative to substantially improve decadal and longer-term projections of ice loss and sea-level rise originating from Thwaites Glacier (https://thwaitesglacier.org/).

Sif Island was visited and circumnavigated by small inflatable boat (zodiac) shortly after its discovery. The main island is ~350 m long and ~120 m wide (Fig. 2). At

https://doi.org/10.1017/S0954102023000287 Published online by Cambridge University Press

the time of the boat landing in February 2020, ~1–2 m of bare bedrock was exposed above the waterline around the island perimeter (Fig. 3), although the tidal state was unknown. Above this bedrock, ~40–50 m-thick snow and ice cover the entire island. The substantial thickness of the snow and ice cover upon the island and the history of ice-margin retreat documented in satellite imagery (Fig. 2) suggest that this cover is an ice-sheet remnant (i.e. dead ice) rather than the result of local snow accumulation alone.

Safe sampling was possible thanks to a small ~100 m^2, ice-free rocky promontory that extends out ~50–60 m away from the main island (Fig. 3b,d). This rose to ~1 m above sea level at the time of landing. The blocky, jointed pink granite cropping out on the promontory is identical in appearance to the rock examined during circumnavigation by zodiac around the perimeter of the main island (Fig. 3). The granite is holocrystalline and has a phaneritic texture. In hand specimen, most visible mineral grains are K-feldpsar, plagioclase, quartz and biotite, typically up to a few millimetres in diameter and approximately equigranular (Fig. 4). Finer-grained regions with a similar mineralogy are also present (Fig. 4b). The bedrock composition and its surface are consistent with geophysical interpretations that hard, crystalline bedrock forms part of the subglacial substrate in this region (Schroeder *et al.* 2014, Muto *et al.* 2019).

Exposed rock surfaces are smooth and lack glacial surface features such as striations (Fig. 4), consistent with low surface ice-flow velocities in the order of just 10 m $year^{-1}$ along the nearby coast (Rignot *et al.* 2014), implying little basal slip. Alternatively, if the promontory only recently emerged above sea level due to isostatic uplift in response to mass loss from the Pine Island Glacier and Thwaites Glacier catchments, the rock surface exposed at present may have previously lain just below the seawater surface, making it vulnerable to wave erosion. This could have removed any glacial surface features and erratics over centuries or millennia prior to uplift. The rock exposure remains low-lying, so it may still be subject to wave erosion at the present day.

Current bed topographies from inversion of ice flow velocities (Morlighem *et al.* 2020) and gravity-derived bathymetric data (Millan *et al.* 2017) show the bed to be below sea level at the location of Sif Island. This highlights that these methods underestimate high-resolution topography, consistent with observed smoothing of data when comparing these datasets to higher-resolution multibeam swath bathymetry data from deglaciated former beds (Hogan *et al.* 2020, Graham *et al.* 2022). These smaller-scale topographic and bathymetric features are important as they can impact basal sliding beneath grounded ice, provide pinning points for ice shelves and also prevent/restrict delivery of warm deep water to the ice-sheet grounding zone and undersides of ice shelves (e.g. Hogan *et al.* 2020).

Analytical methods

Sampling

Samples from Sif Island were obtained from different parts of the accessible exposures, and three samples with designated identifiers SIA, SIB and SIC (SI = Sif Island) were analysed. Sample SIB is shown in Fig. 4d and samples SIA and SIC closely resembled the sample in Fig. 4c.

To determine the time of granite formation, all three rock samples were zircon U-Pb dated using laser ablation inductively coupled plasma mass spectrometry (LA-ICP-MS). Zircon fission track (ZFT) and apatite fission track (AFT) and zircon and apatite (U-Th)/He dating was performed on sample SIA to determine the cooling history of the granite and to gain indirect evidence of the timing of fault activity in the vicinity of Sif Island. Zircon Hf isotope analyses were also conducted. For bulk rock geochemical and radiogenic Nd and Sr isotope analyses, ~230 g of sample SIB was powdered, ensuring a representative bulk sample.

Neodymium and strontium isotopes on bulk rock samples

Analyses were performed on 50 mg of the sample SIB rock powder digested on a hotplate in concentrated HF, $HClO_4$ and HNO_3 for 3–5 days. The samples were processed alongside ~75 mg of United States Geological Survey (USGS) BCR-2 rock standard. The Nd was isolated from the sample matrix using a cation-exchange resin (AG50W-X8, 200–400 μm mesh) and HCl in increasing molarity, followed by a low-molarity HCl Ln-Spec resin procedure (50–100 μm mesh). The sample matrix from the cation-exchange step was dried, taken up in HNO_3 and loaded onto Eichrom Sr Spec resin to wash down the matrix and elute the Sr (Simões Pereira *et al.* 2018).

Neodymium isotopes were measured in the MAGIC laboratories at Imperial College London on a Nu Instruments high-resolution multi-collector inductively coupled plasma mass spectrometer (HR MC-ICP-MS). To account for instrumental mass bias, isotope ratios were corrected using an exponential law and a $^{146}Nd/^{144}Nd$ ratio of 0.7219. Although negligible, interference of ^{144}Sm on ^{144}Nd was corrected for. Bracketing standards were used to correct measured $^{143}Nd/^{144}Nd$ ratios to the commonly used JNdi-1 ratio of 0.512115 (Tanaka *et al.* 2000). USGS BCR-2 rock standard processed alongside the samples yielded measured $^{143}Nd/^{144}Nd$ ratios with a mean of 0.512636 ± 0.000012 (2 SD, $n = 4$), which is within error of the published ratio of 0.512638 ± 0.000015 (Weis *et al.* 2006). A full procedural blank for Nd was 41 pg. $^{143}Nd/^{144}Nd$ ratios are expressed using epsilon notation (ε_{Nd}), which denotes the deviation of a measured ratio from the modern Chondritic Uniform Reservoir (0.512638) in parts per 10 000 (Jacobsen & Wasserburg 1980).

https://doi.org/10.1017/S0954102023000287 Published online by Cambridge University Press

Figure 5. Cathodoluminescence images and U-Pb dates of the 50 zircon grains analysed from sample SIA (SI = Sif Island). Red text indicates discordant ages, and the two Palaeozoic inherited cores are highlighted using green text. Also shown are the ε_{Hf} values (blue text).

Strontium isotopes were measured in the MAGIC laboratories at Imperial College London on a thermal ionization mass spectrometer (TIMS). Samples were loaded in 1 µl of 6 M HCl onto degassed tungsten filaments with 1 µl of $TaCl_5$ activator. The measured $^{87}Sr/^{86}Sr$ ratios were corrected for instrumental mass bias using an exponential law and an $^{88}Sr/^{86}Sr$ ratio of 8.375. Interference of ^{87}Rb was corrected for using an $^{87}Rb/^{85}Rb$ ratio of 0.386. Analyses of the NIST 987 standard reference material yielded a mean of 0.710256 ± 0.000009 (2 SD, $n = 4$), and samples were corrected to the published value of 0.710252 ± 0.000013 (Weis *et al.* 2006). The accuracy of the results was confirmed using rock standard USGS BCR-2 processed alongside the sample, which yielded an $^{87}Sr/^{86}Sr$ ratio of 0.705000 ± 0.00008 (2 SE, $n = 2$), which is within error of the published ratio of 0.705013 ± 0.00010 (Weis *et al.* 2006).

Zircon U-Pb dating

Apatite and zircon grains for all of the geochronological methods described below were concentrated using standard crushing, density separation and magnetic separation techniques at the London Geochronology Centre, University College London, UK, and by ZirChron LLC, Tucson, AZ, USA.

At the London Geochronology Centre, the entire separate was mounted in epoxy resin and 20 zircon grains were analysed from two different rock samples (SIB and SIC). A New Wave Research (NWR) 193 nm laser ablation system coupled to an Agilent 7900 ICP-MS was used. Plešovice zircon was used as a primary standard to correct for instrumental mass bias and depth-dependent inter-element fractionation (Sláma *et al.* 2008), whereas GJ1 zircon was used as a secondary standard to verify the accuracy of the data (Jackson *et al.* 2004). Uranium and thorium concentrations were estimated by comparison with NIST 612 glass (Pearce *et al.* 1997). Data reduction of the time-resolved mass spectrometer data was performed using *GLITTER* 4.5 (Griffin 2008). Although the number of discordant ages was high for sample SIB, the GJ1 ages measured alongside the samples, with a mean

https://doi.org/10.1017/S0954102023000287 Published online by Cambridge University Press

of 612 ± 8 Ma and a range from 604 to 619 Ma, indicate that the data are accurate (Table S1).

Zircon U-Pb dating at the Arizona LaserChron Center used the methods of Gehrels *et al.* (2008) applied to 50 zircon grains selected from sample SIA. Instrumentation comprised a Photon Machines Analyte G2 excimer laser equipped with a HelEx ablation cell using a spot diameter of 20 μm, coupled to an Element2 HR-ICP-MS. Sri Lanka and FC-1 zircon crystals were used as the primary zircon standard reference materials, and R33 zircon crystals were used as a secondary standard. Data reduction was performed in *MATLAB*® using the Arizona LaserChron Center *AgeCalcML* software. Detailed methods are available at www.laserchron.org. Laser spot selection was conducted using colour cathodoluminescence (CL) images generated with a Hitachi 3400N SEM and a Gatan CL2 detector system (www.geoarizonasem.org). These CL images show typical euhedral igneous grains with internal growth zoning.

All final data analyses and visualizations were performed using *IsoplotR* (Vermeesch 2018). Discordant grains were filtered using the log ratio distance to the concordia composition (Vermeesch 2021). Instead of applying a fixed threshold to select between the use of the $^{206}Pb/^{238}U$ ratio or $^{207}Pb/^{206}Pb$ ratio to calculate the age, a single-grain concordia age was calculated. Final ages were calculated as concordia ages.

Zircon Hf isotopes

Methods used for Hf isotope analyses are based on those in Cecil *et al.* (2011) and were conducted at the Arizona LaserChron Centre. Measurements were conducted using a Nu Instruments HR-ICP-MS connected to a Photon Machines Analyte G2 excimer laser. Solutions of 10 ppb of JMC475 and a Spex Hf solution, then 10 ppb solutions containing Spex Hf, Yb and Lu, were used to determine instrument settings. When all solutions yielded $^{176}Hf/^{177}Hf$ ratios of ~0.28216, instrument settings were optimized for laser ablation analyses, and seven different standard zircons (Mud Tank, 91500, Temora, R33, FC52, Plešovice and Sri Lanka) were analysed mounted in the same epoxy pucks. When precision and accuracy were ≤1 unit of ε_{Hf} at the 2σ level, unknowns were analysed using identical acquisition parameters.

Laser ablation pits with a diameter of 40 μm were placed on top of the U-Pb analysis pits, with CL images used to ensure that the ablation pits did not overlap multiple age domains or inclusions (Fig. 5). Each acquisition consisted of one 40 s integration on backgrounds (on peaks with no laser firing) followed by 60 1 s integrations with the laser firing. Using a typical laser fluence of ~5 J/cm^2 and a pulse rate of 7 Hz, the ablation rate is ~0.8 μm/s. Each standard was analysed at the beginning and end of the sample run.

Isotope fractionation was accounted for using the method of Woodhead *et al.* (2004): βHf (mass fractionation factor in the exponential law) was determined from the measured $^{179}Hf/^{177}Hf$; βYb was determined from the measured $^{173}Yb/^{171}Yb$ (except for very low Yb signals). βLu was assumed to be the same as βYb. Ytterbium and Lu interferences were corrected by measurement of $^{176}Yb/^{171}Yb$ and $^{176}Lu/^{175}Lu$ (respectively), as advocated by Woodhead *et al.* (2004). Stable isotope ratios used as reference were $^{179}Hf/^{177}Hf = 0.73250$ (Patchett & Tatsumoto 1980), $^{173}Yb/^{171}Yb = 1.132338$ (Vervoort *et al.* 2004), $^{176}Yb/^{171}Yb = 0.901691$ (Vervoort *et al.* 2004, Amelin & Davis 2005) and $^{176}Lu/^{175}Lu = 0.02653$ (Patchett 1983). All corrections were done line by line. For very low Yb signals, βHf was used for fractionation correction of Yb isotope ratios. The corrected $^{176}Hf/^{177}Hf$ values were filtered for outliers (2σ filter), and the average and standard error were calculated from the resulting ~58 integrations.

The cut-off for using βHf *vs* βYb was determined by monitoring the average offset of the standards from their known values, and the cut-off was set at the minimum offset. This was achieved at ~6 mV of ^{171}Yb. The $^{176}Hf/^{177}Hf$ at the time of crystallization was calculated from measurement of present-day $^{176}Hf/^{177}Hf$ and $^{176}Lu/^{177}Hf$, using the decay constant of ^{176}Lu ($\lambda = 1.867e^{-11}$) from Scherer *et al.* (2001) and Söderlund *et al.* (2004). No capability is provided for calculating Hf-depleted mantle model ages because the $^{176}Hf/^{177}Hf$ and $^{176}Lu/^{177}Hf$ of the source material(s) from which the zircon crystallized are not known. However, a graphical estimate of the model age is made (Fig. S2).

(U-Th)/He dating

(U-Th)/He dating was conducted at the Arizona Radiogenic Helium Dating Laboratory (ARDHL), University of Arizona. This was performed for zircon and apatite grains; the former have a closure temperature range of ~150–200°C (Guenthner *et al.* 2013). Zircon and apatite grains were examined under a polarizing stereo-microscope and selected for (U-Th)/He on the basis of grain size (>60 μm diameter), morphology, clarity and lack of inclusions (Fig. S3). In apatite grains, zircon inclusions containing relatively high concentrations of uranium were common; care was taken to avoid these when picking grains. Final grains were imaged and their dimensions measured, and then they were loaded into Nb packets. To measure He, aliquots were heated with a diode laser to ~1300°C for 18–20 min for zircon and to ~900°C for 4 min for apatite. One or more gas re-extractions (lasing) for

https://doi.org/10.1017/S0954102023000287 Published online by Cambridge University Press

20–21 min at higher temperatures were performed for zircon grains, and no gas re-extracts were done for apatite grains. Extracted He was spiked with ^{3}He, purified using cryogenic and gettering methods and measured with a quadrupole mass spectrometer. A known amount of ^{4}He was measured at every eighth analysis to monitor instrument drift.

Degassed apatite grains were retrieved, spiked with a ^{233}U-^{229}Th-^{147}Sm-^{42}Ca tracer, and dissolved in HNO_3, and U, Th, Sm and Ca isotopes were analysed on an Element2 HR-ICP-MS. Degassed zircon grains were spiked with a ^{233}U-^{229}Th tracer, equilibrated and dissolved in HF in a Parr bomb. The U and Th isotopes of the zircon aliquots were measured on an Element2 HR-ICP-MS. Grain masses were used to calculate U, Th, Sm and He concentrations. For apatite grains, the mass was calculated from Ca measurements and stoichiometry following the protocols of Guenthner *et al.* (2016). For zircon grains, we report the dimensional mass calculated from grain length measurements and assumptions about morphology following the protocols of Hourigan *et al.* (2005). Durango apatite and Fish Canyon tuff zircon were used as standards to assess dissolution protocols and HR-ICP-MS analyses. Blank-corrected (U-Th-Sm)/He and (U-Th)/He ages were calculated with propagated analytical uncertainties from U, Th, Sm and He measurements. Alpha-ejection corrections were applied using grain measurements and assuming apatite and zircon are unzoned with respect to U, Th and Sm (Hourigan *et al.* 2005, Ketcham *et al.* 2011).

The zircon and apatite grains analysed here may have been subject to parentless He contamination from neighbouring U-rich grains or coatings (Murray *et al.* 2014). This probably biased ages to older than the true cooling age, as typically only extreme enrichment of U and Th in zircon rims can lead to ages being biased younger (Hourigan *et al.* 2005), and we observed only minor U zoning when counting fission track densities during ZFT analysis.

Fission track dating

Fission track dating was performed at the Arizona Fission Track Laboratory, University of Arizona. Again, this method was applied to both zircon and apatite grains, with respective closure temperature ranges of ~205 ± 18°C (Bernet 2009) and ~100–120°C (Reiners & Brandon 2006).

For AFT dating, 100 apatite grains were mounted in epoxy resin and polished with alumina powder, and spontaneous fission tracks were revealed by etching with 5.5 M HNO_3 at 21°C (±1°C) for 20 (±0.5) s (Donelick *et al.* 2005). For ZFT dating, 100 zircon grains were mounted in PFA Teflon, diamond polished and etched in an oven at 220°C using a KOH-NaOH eutectic melt (Gleadow *et al.* 1976) in a zirconium crucible for 3–9 h. The optimum fission track etch time is dependent on age and radiation damage and was monitored by repeated etching and observation at 3 h time intervals. Samples were analysed via the external detector method (Gleadow 1981) using very low uranium, annealed muscovite mica detectors and irradiated at the Oregon State University Triga Reactor, Corvallis, OR, USA. The neutron fluence was monitored using European Institute for Reference Materials and Measurements (IRMM) uranium-dosed glasses IRMM 540R for apatite and IRMM 541 for zircon. After irradiation, induced fission tracks in the mica external detectors were revealed by etching with 48% HF at 20°C for 20 min. Spontaneous and induced fission track densities were counted using an Olympus BX61 microscope at 1250× magnification using an automated Kinetek Stage system. Apatite horizontal confined fission track lengths and D_{par} (mean fission track etch pit diameter parallel to the crystallographic *c*-axis) values were measured using *FTStage* software, an attached drawing tube and a digitizing tablet (supplied by Trevor Dumitru of Stanford University) calibrated against a stage micrometer. The apatite uranium concentrations were generally low (average of ~7 ppm), with relatively few fission tracks, meaning only 57 horizontal confined track lengths could be measured. Central ages (Galbraith & Laslett 1993, Galbraith 2005) were calculated using the International Union of Geological Sciences (IUGS) recommended zeta-calibration approach of Hurford & Green (1983). Apatite and zircon IRMM 540R and IRMM 541 weighted mean zeta-calibration factors of 343.1 ± 8.7 and 116.0 ± 0.3, respectively, were obtained by repeated calibration against internationally agreed age standards including Fish Canyon tuff and Durango apatite, as well as Fish Canyon tuff and Tardree rhyolite zircon, according to the recommendations of Hurford (1990).

Inverse thermal history modelling

The fission track and (U-Th)/He dating methods described above constrain the timing and rate of cooling of the sample (Guenthner *et al.* 2013, Ault *et al.* 2019). Such data can be better visualized and interpreted using inverse thermal history modelling; here, this was conducted using the software *QTQt* version 5.8.0 (Gallagher 2012). For the ZFT data, the fission track annealing of Yamada *et al.* (2007) was used. For AFT, the annealing model of Ketcham *et al.* (2007) for 5.5 M etchant was used, with D_{par} as an additional kinetic parameter and initial track length calculated from the compositional (D_{par}) information. The time-temperature ranges for the inverse model prior were set at 89 ± 89 Ma

https://doi.org/10.1017/S0954102023000287 Published online by Cambridge University Press

and 300 ± 300°C, with the maximum allowed heating/cooling rate set at 100°C/Ma. A present-day temperature of 5 ± 5°C is used, as we assume that, until recently, the sample was at the pressure melting point at the base of the ice or in contact with seawater. We also set one constraint box at 175 ± 3 Ma and 575 ± 25°C to allow any thermal history to begin at the granite crystallization age and minimum crystallization temperature. A total of 1 000 000 iterations were run: 500 000 burn-in and 500 000 post-burn-in, with a thinning parameter of 1. We also set *QTQt* to reject proposed models (time-temperature points) outside the initial prior ranges and to reject complex models that do not improve the data fit, with default values used for all other parameters.

The preferred thermal history predicted by *QTQt* is the so-called Expected Model, which is effectively the weighted mean time-temperature path, where the weighting is provided by the posterior probability of post-burn-in accepted models (Gallagher 2012). *QTQt* produces several other model thermal histories, including a maximum likelihood model (the thermal history that best predicts the data, but that is often too complex), a maximum posterior model (the thermal history with maximum probability, but that is generally too simplistic) and a maximum mode model (a thermal history that represents the maximum probability distribution over time and temperature). The latter model tends to be overly complex, but its general trends often provide the most geologically reasonable thermal history, as well as a better fit to the observed data than the Expected Model. Given that *QTQt* will always produce a 'most likely' thermal history regardless of the quality of input data, we made sure to examine the quality of fit between the input data and model predictions made by *QTQt* (Vermeesch & Tian 2014). Our results show that both the Expected and Maximum Mode models predict the measured ZFT and AFT age and length data within 1σ uncertainty.

Major and trace element geochemistry

Approximately 50 mg of the powdered SIB sample was digested in a mixture of concentrated HNO_3, HF and $HClO_4$ in the MAGIC clean laboratories at Imperial College London. Following digestion, samples were diluted to exactly 1000 times the original sample weight in a 2% HNO_3 matrix. Different sample aliquots were digested for major and trace element analyses and isotopic analyses. Concentrations of selected major and trace elements were analysed at the Open University using an Agilent 8800 ICP triple-quadrupole mass spectrometer (see methods in Simões Pereira *et al.* 2018), which includes an integrated collision reaction cell filled with either no gas, He or O_2 to remove isobaric interference ions. Oxide formation (CeO^+/Ce^+) was < 1.03% in no gas mode, and doubly charged species (Ce^{2+}/Ce^+) were < 1.68%. In He mode, oxide formation was < 0.40%, and doubly charged species were < 1.00%. In no gas mode, machine sensitivity varied from 1×10^5 cps/ppb (Li) to 7×10^5 cps/ppb (Y), and in He mode it varied from 5×10^4 cps/ppb (Li) to 1×10^5 cps/ppb (Tl). Measurements were calibrated using USGS reference materials BIR-1, W-2, DNC-1, BHVO-2, AGV-1 and RGM-1 (digested at the Open University), and instrument drift was corrected for using BIR-1. Overall precision (assessed as repeated measurements of a separate digest of BHVO-2 at the Open University) was mainly better than 2% (or 5% for U and Th). The accuracy of the BHVO-2 reference material was predominantly better than 5% (or 10% for Al, Th and U). The BCR-2 standard was processed and measured alongside samples, with elemental concentrations agreeing mostly within 20% (or 37% for Rb).

Cosmogenic nuclides

Satellite imagery suggests that the promontory at Sif Island was ice covered or submerged below sea level until recently (Fig. 2), but the exposure history prior to that time is unknown. We therefore measured the cosmogenic nuclides ^{10}Be (half-life 1.387 ± 0.012 Myr) and *in situ* ^{14}C (half-life 5700 ± 30 years) in quartz from bedrock to investigate the exposure history of Sif Island prior to this most recent, historical deglaciation. Cosmogenic nuclide concentrations are primarily produced by spallation reactions between cosmic ray particles and target nuclei in the uppermost few metres of rock at the surface of the Earth. Cosmogenic nuclides are also produced at much lower rates by muons, both at the surface and up to tens to hundreds of metres depth (e.g. Balco 2017). Concentrations are directly proportional to the time that a surface has been exposed to the cosmic ray flux. As such, cosmogenic nuclides have long been measured in surfaces proximal to Antarctic glaciers to study their past (e.g. Ackert *et al.* 1999).

We note that the bedrock sample used here for cosmogenic nuclide analysis was collected from the ice-free promontory of Sif Island rather than the main island that is currently covered by 40–50 m of ice and snow (Fig. 3). The ^{10}Be concentration was measured in two aliquots and the *in situ* ^{14}C concentration was measured in one aliquot of clean quartz.

Samples for cosmogenic nuclide analysis were processed at Tulane University and Imperial College London. All sample pre-treatment, quartz isolation, cosmogenic nuclide extraction and analysis procedures follow those of Balco *et al.* (2023), with the notable exception that froth flotation was not used to isolate any quartz. To

https://doi.org/10.1017/S0954102023000287 Published online by Cambridge University Press

summarize, samples were crushed and sieved to extract the 125–710 μm grain size fraction, before the magnetic fraction was removed. Quartz was isolated using repeat etching in HF/HNO_3 on a shaker table (in 5% HF/HNO_3) and an ultrasonic bath (in 1% HF/HNO_3) following Nichols & Goehring (2019).

Isotope dilution chemistry and ion-exchange chromatography were used to extract beryllium from the two aliquots of quartz (with masses of 20 and 10 g) following methods similar to Corbett *et al.* (2016). $^{10}Be/^{9}Be$ isotope ratios were measured at the Centre for Accelerator Science, Australian Nuclear Science and Technology Organisation (ANSTO; Wilcken *et al.* 2022). Beryllium was extracted from quartz in this study at the same time as the samples presented in Balco *et al.* (2023) and Nichols *et al.* (2023). In other words, the two aliquots of quartz processed for ^{10}Be analysis in this present study were incorporated into two different batches of samples that were processed in the CosmIC Laboratory at Imperial College London, one of which was composed of samples in Balco *et al.* (2023) and the second of samples in Nichols *et al.* (2023). In Balco *et al.* (2023) and Nichols *et al.* (2023), ^{10}Be concentrations were background corrected using the mean and standard deviation (30 287 ± 8456 atoms) of procedural blanks for the entire series of batches that were processed in succession over a period of a few months. Thus, we use the same background correction for the ^{10}Be concentrations of the Sif Island quartz.

Carbon was extracted from 5 g of quartz for *in situ* ^{14}C analysis using the Tulane University Carbon Extraction and Graphitization (TU-CEGS) system (Goehring *et al.* 2019). $^{14}C/^{12}C$ ratios were measured at the National Ocean Science Accelerator Mass Spectrometry (NOSAMS) facility, stable carbon isotope ratios were measured at the University of California, Davis Stable Isotope Facility and data reduction follows the recommendations of Hippe & Lifton (2014).

The *in situ* ^{14}C blank correction procedure follows that of Balco *et al.* (2023). In short, we measured 49 procedural blanks during the same measurement period as the *in situ* ^{14}C analysis in this present study. Because blanks displayed a positively skewed distribution, we correct *in situ* ^{14}C concentrations by approximating the frequency of blanks using a lognormal distribution fitted to the observed distribution of all blanks.

Sample information and analytical data, including geographical information and measured values required to calculate cosmogenic nuclide concentrations, are found in Tables S2 & S3. The ^{10}Be exposure age discussed below is calculated using version 3 of the online calculators formerly known as the CRONUS-Earth online calculators (Balco *et al.* 2008), along with the Lifton-Sato-Dunai (LSDn) scaling method (Lifton *et al.* 2014) and the 'primary' production

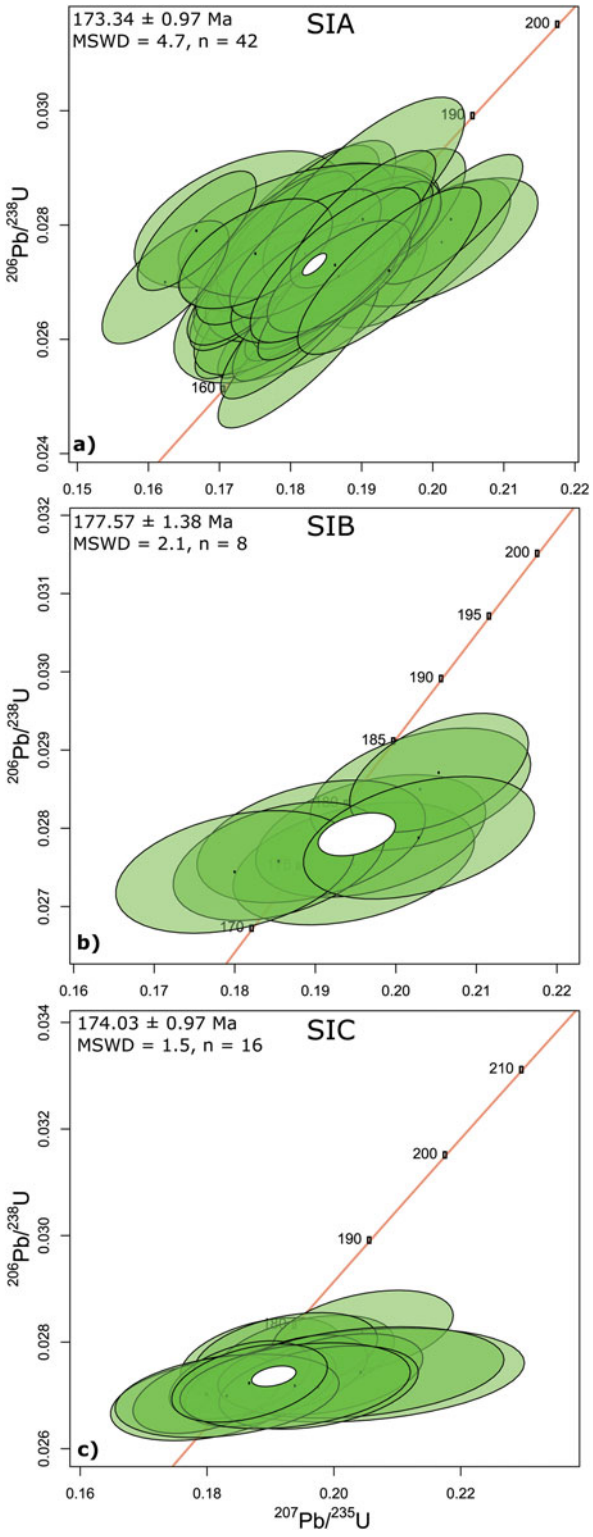

Figure 6. Concordia diagrams for concordant laser ablation inductively coupled plasma mass spectrometer (LA-ICP-MS) U-Pb-dated zircon grains. Data are from samples **a.** SIA, **b.** SIB and **c.** SIC (SI = Sif Island). Concordia ages are presented ±2σ. The combined equivalence and concordance mean of the squared weighted deviates (MSWD) is reported as well as the number of concordant grains (*n*).

https://doi.org/10.1017/S0954102023000287 Published online by Cambridge University Press

Table I. Sif Island granite apatite and zircon fission track data. ρ_s = spontaneous track density, ρ_i = induced track density and ρ_d = dosimeter track density. N_s, N_i and N_d are the respective track counts. Very low age dispersion percentages indicate that all of the data for each method are close to identical. $P\chi^2$ is the probability of obtaining a χ^2 value for v degrees of freedom where v = no. of crystals – 1. SE = standard error.

Mineral	No. of crystals	Track density ($\times 10^6$ tracks cm^{-2}) ρ_s (N_s)	ρ_i (N_i)	ρ_d (N_d)	Age dispersion ($P\chi^2$)	Central age (Ma) (±1σ)	Apatite mean track length (μm ± 1 SE) (no. of tracks)	Standard deviation (μm)
Apatite	40	0.2386 (433)	0.7735 (1404)	1.746 (5587)	< 0.01% (99.9%)	91.7 ± 5.7	14.30 ± 0.10 (57)	0.71
Zircon	20	14.56 (3280)	2.582 (798)	0.5125 (3280)	< 0.01% (99.4%)	165.5 ± 7.2	-	-

rate calibration dataset (Borchers *et al.* 2016). The ^{10}Be exposure age is an apparent exposure age because we assume no erosion and constant surface exposure.

Scanning electron microscope modal mineralogy

Modal mineralogy data were collected using a Tescan Tima scanning electron microscope (SEM) system at the Natural History Museum, London. This instrument is equipped with four EDAX Element 30 energy-dispersive X-ray spectroscopy (EDS) detectors and was operated at 25 kV accelerating voltage and 14 nA probe current. Mineralogy was determined by conducted EDS analysis at a 7 μm pixel resolution. A separate backscattered image was acquired at a 0.5 μm pixel resolution. Mineral classifications were created based on spectra acquired from this sample.

Results

SEM mineralogy

Mineral abundances inferred from the elemental analysis suggest the Sif Island rocks have a typical granite composition, dominated by quartz (~33%), K-feldspar (~29%) and plagioclase (~32%; Table S4). The K-feldspar is typically perthitic. When plotted on a quartz-alkali feldspar-plagioclase-feldspathoid (QAPF) diagram, the modal analysis confirms that the sample is a granite. The accessory minerals present are also typical for a granite. Although elemental data acquired from the SEM are only qualitative, they suggest percentages of SiO_2 (~73%), Na_2O (~4%) and K_2O (~5%) in line with those expected for a granite.

Geochronology and low-temperature thermochronology

LA-ICP-MS zircon U-Pb dating of samples SIA, SIB and SIC gave weighted mean single-grain concordia ages of 173.3 ± 1.0, 177.6 ± 1.4 and 174.0 ± 1.0 Ma, respectively (Fig. 6 & Table S1). The Sif Island granite therefore formed at ~177–174 Ma. The CL images show discontinuities in zoning in some grains; for example, grain 20 may show some resorption suggestive of slow, complex magma crystallization (Fig. 5). Dark areas, typical of higher U concentrations, are also visible (Fig. 5). The cores of grains 15 and 36 are particularly dark, which would support these younger ages being caused by Pb loss due to high radiation damage. Furthermore, despite a different texture not being obvious in the CL images, two concordant cores from sample SIA appear to be inherited, with ages of 305.1 ± 8.9 and 380.5 ± 14.6 Ma (Fig. 5 & Table S1). This implies that partial melting of Palaeozoic granitoids contributed to the melt.

Following emplacement, the thermochronological data permit evaluation of the timing and rate of cooling through zones of crustal closure temperature, T_c (see temperature ranges referenced in the 'Analytical methods' section). After emplacement and crystallization of the Sif Island granite at ~177–174 Ma, a period of rapid cooling is recorded by our ZFT date of 165.5 ± 7.2 Ma, which records the time of cooling through the ZFT T_c (~205 ± 18°C). This implies that the Sif Island granite cooled to < ~200°C within ~20 million years of formation by exhumation, thermal relaxation or some combination thereof.

Zircon (U-Th)/He (ZHe) and AFT dates provide closure temperature constraints at slightly cooler temperatures, with respective T_c ranges of ~150–200°C and ~100–120°C. The Sif Island granite contained one zircon grain with a ZHe alpha-ejection-corrected age of 92.3 ± 1.3 Ma (Table S5) and has an AFT central age of 91.7 ± 5.7 Ma (Table I). The close agreement of these thermochronometers suggests rapid cooling at ~100–90 Ma through the ZHe and AFT T_c ranges. Rapid cooling at ~100–90 Ma is supported by relatively long apatite-confined fission track lengths (mean 14.30 μm; Fig. 7c).

Except for the single 92.3 ± 1.3 Ma ZHe date, all other apatite (U-Th)/He (AHe) and ZHe dates for the Sif Island granite were older than the zircon U-Pb dates, which is impossible given the much warmer temperature sensitivity of the zircon U-Pb system. This 'age inversion' is likely to be a consequence of contamination from neighbouring U-rich grains or coatings ('bad neighbours') injecting parentless He into the apatite and zircon grains. This hypothesis is supported by an

https://doi.org/10.1017/S0954102023000287 Published online by Cambridge University Press

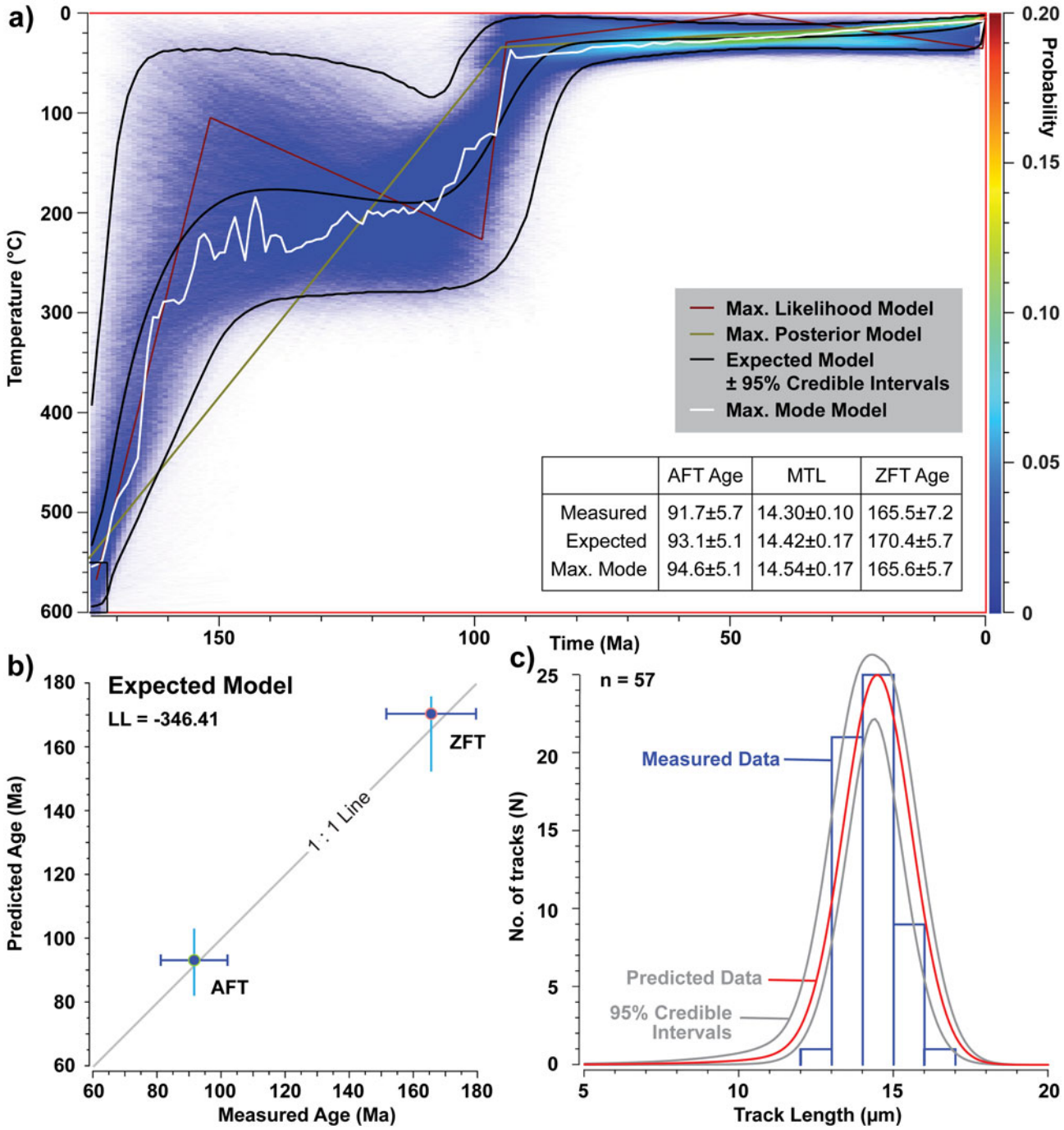

Figure 7. Thermal history of the Sif Island granite. Panel **a.** shows the *QTQt* temperature paths. Following crystallization (~177–174 Ma), there was rapid cooling, followed by another period of rapid cooling at ~100–90 Ma. **b.** Comparison of the expected model age and measured age for the two thermochronometers applied. Panel **c.** shows the measured fission track length data as a histogram (blue), overlain by the modelled fission track data (grey and red). Note that although the zircon (U-Th)/He (ZHe) date for the grain with an age of 92.3 ± 1.3 Ma may be accurate, we do not include this date in the thermal history modelling. AFT = apatite fission track; LL = log likelihood; MTL = mean track length (in micrometres); ZFT = zircon fission track.

anti-correlation between dates of grains and effective uranium concentrations (Tables S5 & S6), as well as high concentrations of fission tracks at the edges of apatite grains (Fig. S1). We note that 'bad neighbours' will not impact the fission track data, as fission tracks are physical features in the grain and any tracks 'injected' from outside the grain will only be seen on the outer edge and can easily be avoided when counting (Fig. S1).

https://doi.org/10.1017/S0954102023000287 Published online by Cambridge University Press

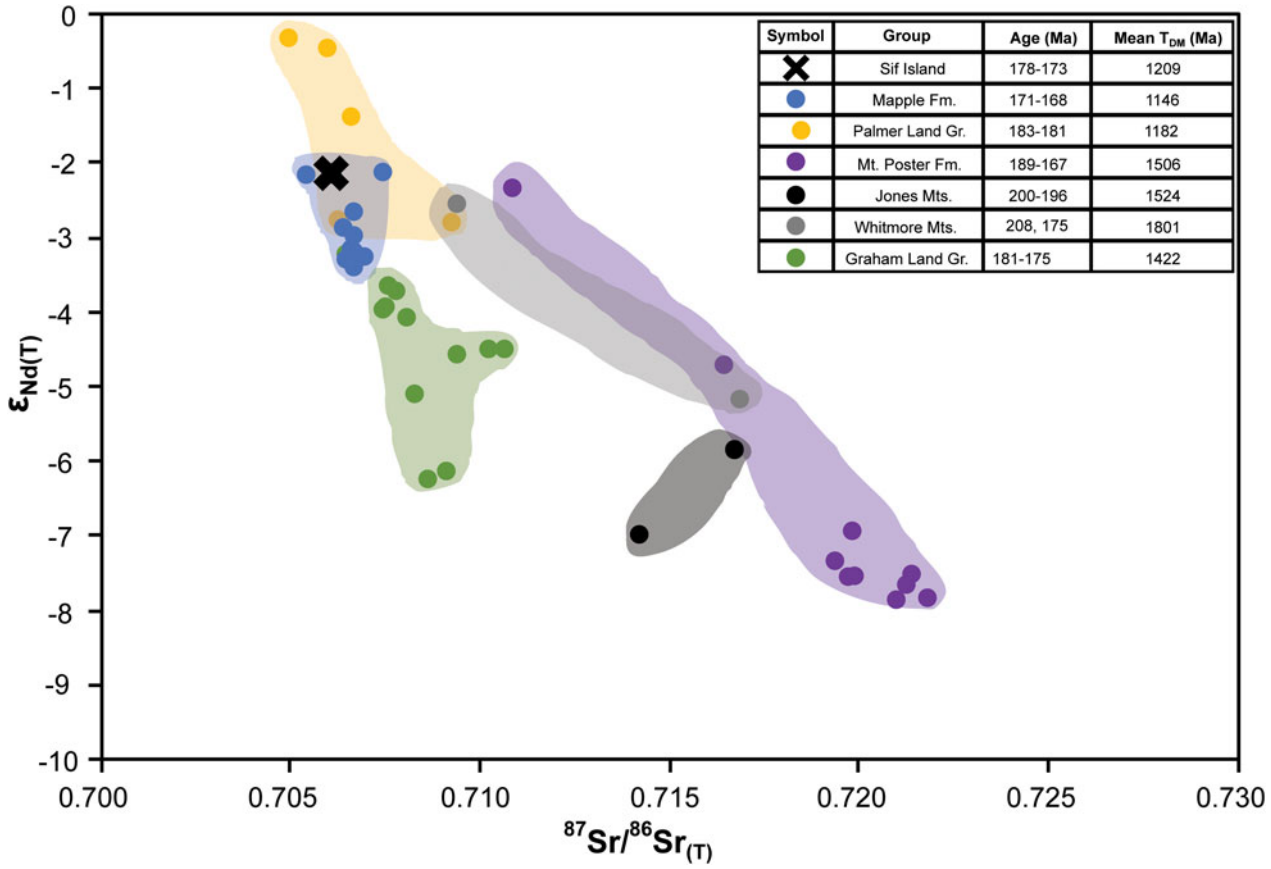

Figure 8. Initial Nd and Sr isotopic composition of the Sif Island granite (black cross) compared to the isotopic composition of other late Early Jurassic rocks (~190–170 Ma) calculated at $T = 174$ Ma. These include the Mapple Formation in eastern Graham Land (blue; isotopic data from Riley *et al.* 2001), with sensitive high-resolution ion microprobe (SHRIMP) ages of 171–168 Ma (Pankhurst *et al.* 2000); the Mount Poster Formation in southern Palmer Land (purple; isotopic data from Riley *et al.* 2001, Bastias *et al.* 2021) with U-Pb zircon ages of ~189–167 Ma (Fanning & Laudon 1997, 1999, Bastias *et al.* 2021); the Jones Mountain granites (black), with a Rb-Sr age of 198 ± 2 Ma (Pankhurst *et al.* 1993); the Whitmore Mountain granite (grey), zircon U-Pb dated to 175 and 208 Ma (Craddock *et al.* 2017); Palmer Land granitoids (yellow), Sr and zircon U-Pb dated to 183–181 Ma (Wareham *et al.* 1997, Millar *et al.* 2001, Bastias *et al.* 2021); and Graham Land granitoids (green), Sr dated to 181–175 Ma (Millar *et al.* 2001). Also shown are recalculated Nd-depleted mantle model ages (T_{DM}). These data show a much closer agreement between the Sif Island granite and the Mapple Formation and Palmer Land granitoids than other Early-Middle Jurassic rocks.

Despite the 'bad neighbour' issue, we judge that the analysed zircon grain with a ZHe date of 92.3 ± 1.3 Ma escaped this effect and that its (U-Th)/He-corrected age is reliable. This is because only extreme enrichment of U and Th in zircon rims, which was not observed when counting fission tracks, can lead to ages being biased younger than the true cooling age. Furthermore, since the ZHe T_c falls between the ZFT and AFT T_c ranges, a ZHe date (92.3 ± 1.3 Ma) slightly older than the AFT date (91.7 ± 5.7 Ma) from the same sample is geologically reasonable. To avoid basing interpretations on a single grain, we do, however, exclude this ZHe date from our inverse thermal history modelling.

Inverse thermal history modelling

The cooling history of the Sif Island granite can be visualized and investigated further using *QTQt* inverse thermal history modelling (Fig. 7). For the early post-crystallization history, the probability density distribution of acceptable time-temperature paths (shown by the colour map and maximum mode model path in Fig. 7) is constrained by the ZFT annealing model (see 'Analytical methods' section). The modelling shows that the Sif Island granite cooled relatively quickly following emplacement at 177–174 Ma to temperatures < ~280°C by ~160 Ma (Fig. 7). It then remained at temperatures of ~180–280°C until the onset of rapid cooling between ~100 and 90 Ma, during which time temperatures rapidly cooled to < ~50°C. However, inverse thermal history modelling is unable to reveal the cause of rapid cooling. It cannot, therefore, discern whether the rapid cooling at ~100–90 Ma was due to thermal relaxation following a period of elevated heat flow or to bedrock cooling caused by rapid exhumation.

https://doi.org/10.1017/S0954102023000287 Published online by Cambridge University Press

Table II. Bulk rock neodymium and strontium isotope data for sample SIB (SI = Sif Island), including a full procedural replicate from the powdered sample. Initial compositions (i) are calculated at 174 Ma. Epsilon values assume a modern $^{143}Nd/^{144}Nd$ of 0.512638 (Jacobsen & Wasserburg 1980). The $^{147}Sm/^{143}Nd$ ratio is calculated from the rock's elemental composition (Table IV). The 2 standard error (SE) values represent internal measurement error. The 2 standard deviation (SD) values are the reproducibility of the $^{143}Nd/^{144}Nd$ ratio of the JNdi-1 standard during the run (0.512136 ± 15; $n = 19$). Neodymium model ages (T_{DM}) are calculated relative to the modern depleted mantle using a single-stage evolution model with a $^{147}Sm/^{143}Nd$ ratio of 0.2136 and a $^{143}Nd/^{144}Nd$ ratio of 0.51315.

Sample	$^{143}Nd/^{144}Nd$	ε_{Nd}	±2σ SE	±2 SD	$^{147}Sm/^{144}Nd$	$^{143}Nd/^{144}Nd_{(i)}$	$\varepsilon_{Nd(i)}$	T_{DM} (Ma)	$^{87}Sr/^{86}Sr$	$^{87}Rb/^{86}Sr$	$^{87}Sr/^{86}Sr_{(i)}$	±2σ SE
SIB	0.512432	-4.02	0.000008	0.29	0.1240	0.512291	-2.40	1220	0.725175	7.714	0.706091	0.000008
Replicate	0.512446	-3.75	0.000010	0.29	0.1240	0.512305	-2.13	1197	0.725184	7.714	0.706100	0.000007

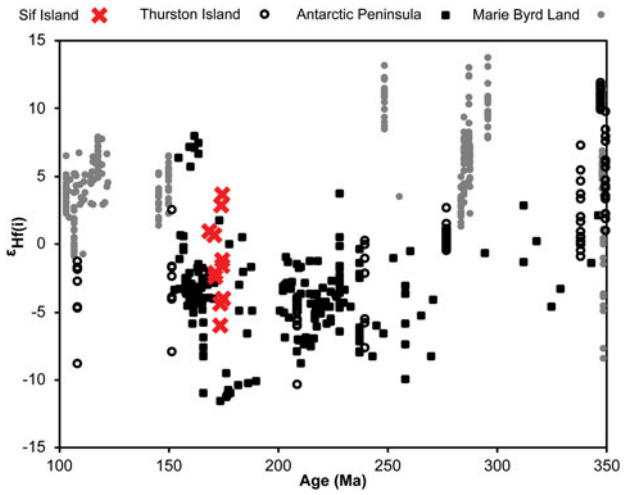

Figure 9. Initial Sif Island ε_{Hf} data (red crosses) compared to literature data from Thurston Island (hollow black circles; Riley *et al.* 2017, Nelson & Cottle 2018), the Antarctic Peninsula (black squares; Flowerdew *et al.* 2006, Bastias *et al.* 2020, 2021) and eastern Marie Byrd Land (grey circles; Nelson & Cottle 2018). The Sif Island granite falls within the range of values from Antarctic Peninsula and Thurston Island samples, whereas different $\varepsilon_{Hf(i)}$ values and a lack of magmatism in the Early-Middle Jurassic are apparent in the data from Marie Byrd Land.

The absence of meaningful AHe data makes it difficult to constrain the more recent, lowest-temperature evolution of the Sif Island granite after the rapid cooling in the mid-Cretaceous. However, the lack of any resetting or partial resetting of AFT ages or lengths since ~85 Ma limits total cooling of the current sea-level exposure level of the Sif Island granite to < ~50°C since this time.

Neodymium, strontium and hafnium isotope composition

The $^{143}Nd/^{144}Nd$ ratio grants insight into the initial magma composition and, in combination with Sm and Nd concentrations, to the probable mantle separation age of a rock (i.e. Nd model age). The mean modern ε_{Nd} value for Sif Island is -3.9 and the calculated mean initial value is -2.3 (Fig. 8 & Table II). The $^{87}Sr/^{86}Sr$ ratio of the Sif Island granite was initially 0.7061 but is now unusually high (0.7252) compared to the ε_{Nd} value due to a high Rb/Sr ratio (Fig. 8 & Tables II & IV). The mean Nd model age is 1209 Ma.

Zircons in the Sif Island granite have a mean εHf_i value of -1.3 ± 2.9 (1 S.D.), evenly distributed between extremes of -6.0 and +3.7 (Fig. 9 & Tables III & S7). The zircon Hf model age is ~1100 Ma (Fig. S2). Both Nd and Hf model ages therefore suggest a contribution from an older, 'Grenvillian'-age crustal source.

Major and trace element composition of the Sif Island granite

The elemental concentration data show that the Sif Island granite has a light rare Earth element (REE) enrichment ($La_N/Lu_N = 7.10$). The Sif Island granite also displays a strong negative Eu anomaly of 0.32 ($Eu/Eu^* = Eu/[Sm + Gd]^{1/2}$) when normalized to chondrites (Fig. 10). Compared to rocks from islands on the northern side of Pine Island Rift (grey in Fig. 10), the Sif Island granite is rich in Rb, Th, U, Pb, Sm, Gd, Tb, Dy, Ho, Er, Tm and Yb and poor in Sr, Ti, Mn and Fe (Table IV).

Cosmogenic nuclides

Two aliquots of the same quartz yielded 77 607 ± 3876 and 36 241 ± 3610 (1σ) total ^{10}Be atoms, statistically significantly above the background of 30 282 ± 8454 total ^{10}Be atoms (mean ± 1 SD of process blanks; Table S2). After background correction and error propagation in quadrature, the resulting ^{10}Be concentrations in the two aliquots are 2363 ± 662 and 593 ± 939 atoms g^{-1} (1σ; Table S2); these two analyses are statistically indistinguishable within the uncertainties and therefore reproducible. The average concentration of the two aliquots, 1775 ± 541 ^{10}Be atoms g^{-1} (weighted mean ± 1 SE), is used as the best estimate of the ^{10}Be concentration in the Sif Island granite quartz.

Additionally, we extracted *in situ* ^{14}C (one analysis) from the same quartz, resulting in a concentration of 55 840 ± 1296 atoms g^{-1} (Table S3). This *in situ* ^{14}C concentration is higher than is realistic and therefore

https://doi.org/10.1017/S0954102023000287 Published online by Cambridge University Press

Table III. Zircon hafnium isotope data for sample SIA (SI = Sif Island). Grain numbers correspond to cathodoluminescence images in Fig. 5. The initial $^{176}Hf/^{177}Hf$ ratio was calculated from the measurement of present-day $^{176}Hf/^{177}Hf$ and $^{176}Lu/^{177}Hf$ ratios using the decay constant of ^{176}Lu ($\lambda = 1.867e^{-11}$) from Scherer *et al.* (2001) and Söderlund *et al.* (2004). For the estimation of the Hf model age, see Fig. S2. The 1σ errors on the $^{176}Hf/^{177}Hf$ ratio are internal measurement 1 standard errors. Grain ages were determined using the U-Pb method (Table S3).

Grain no.	$(^{176}Yb + ^{176}Lu)/^{176}Hf$ (%)	Volts Hf	$^{176}Hf/^{177}Hf$	±1σ	$^{176}Lu/^{177}Hf$	$^{176}Hf/^{177}Hf_{(t)}$	ε_{Hf}	±1σ	$\varepsilon_{Hf(i)}$	Grain age (Ma)	±1σ
2	22.456	2.279	0.282702	0.000028	0.001241	0.282698	-2.9	1.0	0.7	170.4	4.0
6	25.977	2.366	0.282712	0.000023	0.001496	0.282707	-2.6	0.8	1.0	168.2	3.0
10	31.305	2.447	0.282514	0.000025	0.001863	0.282507	-9.6	0.9	-6.0	173.1	2.5
11	24.248	1.904	0.282624	0.000021	0.001459	0.282619	-5.7	0.7	-2.1	170.9	3.9
13	23.156	2.059	0.282565	0.000022	0.001386	0.282561	-7.8	0.8	-4.0	174.5	2.6
18	29.495	2.248	0.282635	0.000030	0.001745	0.282630	-5.3	1.1	-1.6	174.2	3.2
20	23.479	2.051	0.282647	0.000019	0.001445	0.282642	-4.9	0.7	-1.2	174.1	3.1
22	30.408	1.961	0.282636	0.000034	0.001929	0.282630	-5.3	1.2	-1.6	174.0	3.7
24	23.840	2.493	0.282615	0.000020	0.001496	0.282610	-6.0	0.7	-2.4	171.1	3.7
42	30.832	1.852	0.282785	0.000018	0.001834	0.282779	0.0	0.6	3.7	174.3	2.9
49	22.670	2.342	0.282763	0.000033	0.001570	0.282758	-0.8	1.2	2.9	173.6	3.5
50	45.559	2.040	0.282560	0.000025	0.002465	0.282552	-7.9	0.9	-4.4	173.4	3.8

Table IV. Selected major and trace element concentrations for the Sif Island granite sample SIB. The results from two procedural replicates and mean values are shown.

	Sample		
Element	SIB	Replicate	Mean
Major elements (%)			
Al	7.58	7.76	7.67
Ca	0.64	0.65	0.64
Ti	0.09	0.10	0.10
Mn	0.03	0.03	0.03
Fe	1.00	0.99	1.00
Trace elements (ppm)			
Sc	4.49	4.49	4.49
V	5.34	5.43	5.39
Rb	251.9	252.1	252.0
Sr	94.46	94.95	94.70
Mo	0.36	0.35	0.36
Ba	611.3	607.5	609.4
La	31.83	31.62	31.73
Ce	65.13	65.74	65.43
Pr	7.38	7.40	7.39
Nd	26.85	27.09	26.97
Sm	5.51	5.56	5.53
Eu	0.54	0.54	0.54
Gd	4.75	4.74	4.75
Tb	0.79	0.78	0.78
Dy	4.73	4.72	4.73
Ho	0.99	0.99	0.99
Er	2.94	2.93	2.94
Tm	0.48	0.48	0.48
Yb	3.13	3.14	3.14
Lu	0.46	0.47	0.46
Re	0.00	0.00	0.00
^{208}Pb	33.24	32.94	33.09
Th	19.87	19.86	19.87
^{238}U	5.67	5.57	5.62

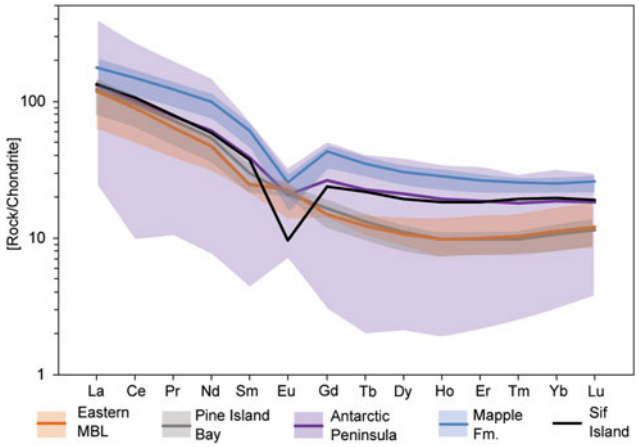

Figure 10. Rare Earth element composition of the Sif Island granite (this study, black) in comparison to rocks from eastern Marie Byrd Land (MBL; orange; Kipf *et al.* 2012), northern Pine Island Bay (grey; Kipf *et al.* 2012), Triassic–Jurassic volcanic and plutonic rocks from the Antarctic Peninsula (purple; Bastias *et al.* 2021) and the Mapple Formation in eastern Graham Land (blue; Riley *et al.* 2001). The data have been normalized to chondrites (McDonough & Sun 1995). Means are shown as thick lines, with the range in samples shown as shaded regions.

cannot be used as an indicator of Holocene exposure of Sif Island. The high concentration is probably an indicator that our pre-treatment protocol (e.g. Nichols & Goehring 2019) did not sufficiently remove meteoric ^{14}C from this sample. We speculate that endolithic algae or marine organisms could have supplied meteoric ^{14}C in the form of carbonate/bicarbonate to the sample because the Sif Island promontory was either underwater or under ice on the coast.

Discussion

Exposure history

Because of the complexities of the *in situ* ^{14}C data, our interpretation of Sif Islands exposure history is limited to the ^{10}Be results (Table S2). The measured average

https://doi.org/10.1017/S0954102023000287 Published online by Cambridge University Press

^{10}Be concentration could result from surface or subsurface nuclide production or, more likely, a combination of the two.

If the measured ^{10}Be concentration was produced entirely during surface exposure and neglecting any erosion, the exposure would have had a duration of 337 ± 105 years (1σ external error). However, this 'end-member' exposure scenario alone cannot explain the measured ^{10}Be concentration, as the Sif Island promontory was probably overlain by ice (or seawater) until more recently (Fig. 2). An alternative 'end-member' scenario assumes that the measured ^{10}Be concentration was produced entirely due to subsurface nuclide production. In this scenario, if enough time has elapsed, production by muons at significant depth beneath ice or seawater can reach secular equilibrium between production and radioactive decay. The average ^{10}Be concentration would be equivalent to muon production under ~350 m of ice (at either 0 or 400 m above sea level), or slightly less seawater, over millions of years (Balco *et al.* 2023). In either of these scenarios, we assume no subglacial erosion, which is arguably an improbable assumption when considering timescales of millions of years and subglacial erosion processes during multiple glacial-interglacial cycles. However, erosion rates are likely to be relatively low on the island given the cold climate, limited basal slip and hard granitic bedrock (Fernandez *et al.* 2016).

The measured ^{10}Be concentration of the Sif Island granite is unlikely to be the result of purely subaerial exposure over 337 ± 105 years or purely burial under ~350 m of ice for millions of years. However, with only one cosmogenic nuclide measurement, we cannot determine the combination of exposure and burial history that produced the measured concentration. Instead, we speculate that the measured ^{10}Be concentration is a function of some combination of thicker than present ice cover during glacial periods, periodic exposure during past warm periods of the Pleistocene/Pliocene and/or subglacial erosion. Future work involving the measurement of multiple cosmogenic nuclides and/or from multiple depths in the subsurface (e.g. from a bedrock core) would be needed to address the equifinality of these initial results.

Thermal history and structural control of Pine Island Rift

More conclusive inferences can be made regarding the cooling history of the Sif Island granite. Following plutonic emplacement at ~177–174 Ma, the thermal history of the Sif Island granite broadly resembles that of pre-Jurassic basement rocks from Thurston Island (Zundel *et al.* 2019b). These rocks record cooling in the latest Early Jurassic, followed by a period of relative thermal stability and a second episode of cooling in the Early Cretaceous. The timing of Jurassic emplacement and cooling at Sif Island does, however, slightly lag the Early Jurassic cooling recorded in the Thurston Island rocks, as the Sif Island granite was intruded at the peak of the cooling recorded on Thurston Island (~175 Ma).

At Sif Island, the Late Jurassic and Early Cretaceous period of relative thermal stability was followed by rapid cooling between ~100 and 90 Ma (Fig. 7). This is a near ubiquitous cooling episode recorded in rocks along the entire length of the palaeo-Pacific margin of West Antarctica (Richard *et al.* 1994, Adams *et al.* 1995, Storey *et al.* 1996, Lisker & Olesch 1998, Lindow *et al.* 2016, Spiegel *et al.* 2016, Zundel *et al.* 2019a,b). This cooling episode has been proposed to be broadly a consequence of a switch from convergence to extension, potentially due to an ocean ridge or the Hikurangi Plateau colliding with the subduction zone (Mukasa & Dalziel 2000, Lindow *et al.* 2016, Spiegel *et al.* 2016, Nelson & Cottle 2018, Zundel *et al.* 2019b, Jordan *et al.* 2020). From ~115 to 90 Ma, extension occurred in Marie Byrd Land (McFadden *et al.* 2010), central West Antarctica (Jordan *et al.* 2020), the Ross Sea sector (Siddoway *et al.* 2004) and the Campbell Plateau and Zealandia (Tulloch *et al.* 2019), leading to extensive magmatism in Marie Byrd Land and the West Antarctic Rift System (e.g. Jordan *et al.* 2020). Cooling linked to this extension began in Marie Byrd Land at ~105–100 Ma (McFadden *et al.* 2015, Zundel *et al.* 2019a) and had progressed towards Thurston Island by ~95 Ma (Zundel *et al.* 2019b). The cooling has been attributed to gravitational orogenic collapse (Lindow *et al.* 2016) or tectonic denudation (Spiegel *et al.* 2016).

The new data from Sif Island allow assessment of the role of Pine Island Rift during this regional switch from convergence to extension. By comparing cooling histories from Sif Island on the southern side of Pine Island Rift (Fig. 7) to published data from granitoids on the northern side (Lindow *et al.* 2016), our data show that there was offset along Pine Island Rift at ~100–90 Ma. This is because, prior to the rapid cooling at ~100–90 Ma, the Sif Island granite was at temperatures below the ZFT T_c (Fig. 7), whereas rocks from the northern flank of Pine Island Rift were at higher temperatures above the sensitivity of the ZFT T_c (Lindow *et al.* 2016). The southern flank of Pine Island Rift (i.e. Sif Island) was therefore at significantly lower temperatures than the northern flank at ~100 Ma. However, both sides of the rift cooled to similar temperatures of < ~50°C following the rapid cooling (i.e. after ~90 Ma), equivalent to < ~1 km depth assuming a geothermal gradient similar to the present day (Dziadek *et al.* 2021). The southern side of Pine Island Rift with Sif Island must therefore have been subject to less uplift, requiring vertical offset along the fault.

https://doi.org/10.1017/S0954102023000287 Published online by Cambridge University Press

Our data thus indicate an early Late Cretaceous age for most of the vertical offset along Pine Island Rift. This represents the first robust geological evidence to support geophysical studies suggesting that Pine Island Glacier lies on a major tectonic structure that was active in the Cretaceous (i.e. Pine Island Rift; Jordan *et al.* 2010, Gohl 2012, Gohl *et al.* 2013), as previous data have only constrained the cooling history on one flank of Pine Island Rift (Lindow *et al.* 2016). We note that this does not preclude later Cenozoic activity along Pine Island Rift, although this must have been comparatively limited given the similar AFT ages on both sides.

We can also estimate the minimum magnitude of offset along Pine Island Rift at ~100–90 Ma. While the absolute temperature bounds of the ZFT partial annealing zone can vary dependent on radiation damage (e.g. Reiners & Brandon 2006), field-based estimates of the temperature range suggest it spans at least 60–80°C (Bernet *et al.* 2009, Rahn *et al.* 2019). This would represent a physical vertical offset of at least 1 km assuming a high geothermal gradient of 60–65°C/km, as estimated for Pine Island Bay granitoids in the Early Cretaceous (Mehling 2015).

The observed cooling at ~100–90 Ma precedes the break-up of West Antarctica and Zealandia, which occurred at ~88–83 Ma along this sector of the former Pacific-Gondwana margin (Larter *et al.* 2002, Riefstahl *et al.* 2020). Along the Antarctic Peninsula, there were significant changes to convergence rates at ~95 Ma (Twinn *et al.* 2022), with subduction probably oblique to the plate boundary (McCarron & Larter 1998, Larter *et al.* 2002). The extension along Pine Island Rift may be linked to plate motion resulting from oblique dextral subduction along the Antarctic Peninsula at this time (McCarron & Larter 1998).

Comparisons to surrounding crustal blocks

The new data from the Sif Island granite can assign this crust to a tectonic province, reducing uncertainty regarding the position of the boundaries between West Antarctic crustal blocks in the Amundsen Sea sector. The granite's age provides the first clue. Evidence for Jurassic magmatism dating to ~190–170 Ma is notably lacking along the coast of Marie Byrd Land (Riley *et al.* 2017; Fig. 9) and is rare in detritus shed from Thwaites Glacier (Fig. 1; Simões Pereira *et al.* 2020). On the other hand, rocks of Early-Middle Jurassic age (~180–170 Ma) are present in the Antarctic Peninsula and the Thurston Island crustal blocks (e.g. Pankhurst *et al.* 2000, Millar *et al.* 2001, Riley *et al.* 2017, Bastias *et al.* 2021). In the Pine Island Bay area, Jurassic magmatism is recorded in granitoids of the Brownson Islands and Edwards Islands (Fig. 1) that have zircon U-Pb ages clustering around ~165 and ~194 Ma (Mukasa & Daziel 2000). Further north and east, the Antarctic Peninsula contains widespread outcrops of Jurassic silicic igneous rocks, although they are predominantly extrusive. The ~177–174 Ma Sif Island granite formed during a pause in Antarctic Peninsula silicic magmatism (Pankhurst *et al.* 2000, Bastias *et al.* 2021) or perhaps at the very start of a subsequent magmatic phase at ~173–160 Ma (labelled V2 by Pankhurst *et al.* 2000), which nearly overlaps with the youngest U-Pb zircon age of the Sif Island granite (173.3 Ma). These Antarctic Peninsula V2 rocks may have formed in a continental arc setting (Bastias *et al.* 2021). The Jurassic emplacement age of the Sif Island granite therefore supports it belonging to the Thurston Island/Antarctic Peninsula crustal block.

The isotopic data of the Sif Island granite corroborate this hypothesis, as they display similarities to Antarctic Peninsula rocks. Comparing the initial $^{87}Sr/^{86}Sr$ ratio of 0.7061 and ε_{Nd} value of -2.3 of Sif Island to rocks of similar Early-Middle Jurassic age reveals similarity to granitoids in north-western Palmer Land (Millar *et al.* 2001, Bastias *et al.* 2021) and other rocks on the Antarctic Peninsula (Wever *et al.* 1994, Scarrow *et al.* 1996, Riley *et al.* 2001) (Fig. 8 & Table S8). These rock types also have a similar Nd mantle separation age to that of Sif Island (~1200–1100 Ma). Furthermore, zircon hafnium isotope data corroborate a match with Antarctic Peninsula and Thurston Island tectonic development, matching the range of values observed here through the Jurassic (Fig. 9 & Table S9; Flowerdew *et al.* 2006, Riley *et al.* 2017, Nelson & Cottle 2018, Bastias *et al.* 2020, 2021), which has been linked to the extensional tectonic setting (Nelson & Cottle 2018).

The Mapple Formation of the Antarctic Peninsula consists of felsic extrusive rocks formed during the V2 phase, which are suggested to have formed through partial melting of andesitic Grenville-aged lower crustal rocks (Pankhurst & Rapela 1995, Riley *et al.* 2001, Bastias *et al.* 2021). The Sif Island granite may have crystallized from a shared parent magma, hypothesized to have an isotopically uniform $^{87}Sr/^{86}Sr_i$ ratio of ~0.707 and $\varepsilon_{Nd(i)}$ value of ~-3 (Riley *et al.* 2001). Similarity with such a magma is supported by the bulk geochemical data, revealing a similar light REE enrichment (La_N/Lu_N) for Sif Island (7.10) as in samples from the Mapple Formation (mean of 6.80; Riley *et al.* 2001) and other Antarctic Peninsula igneous rocks (mean of 7.14; Bastias *et al.* 2021). The Sif Island granite also has a negative Eu*/Eu anomaly, which is consistent with these rock groups (Fig. 10). Jurassic igneous rocks along the Antarctic Peninsula contain evidence for a subduction-derived component (Bastias *et al.* 2021). The Sif Island granite has similar isotopic and elemental compositions and may have been emplaced in a continental margin arc, contemporaneous

https://doi.org/10.1017/S0954102023000287 Published online by Cambridge University Press

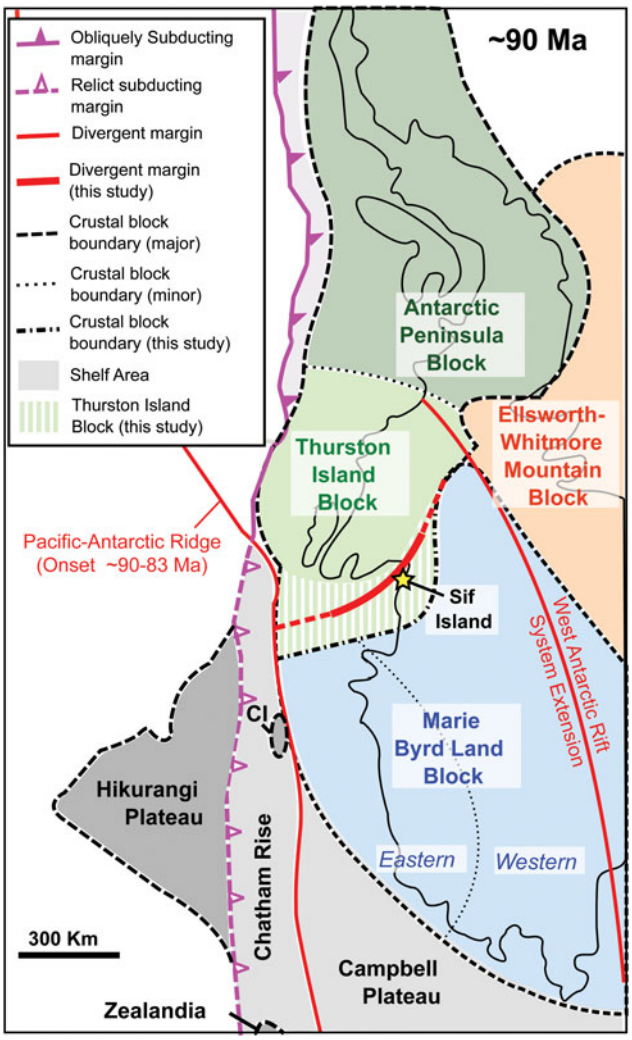

Figure 11. The configuration of the crustal blocks at tectonic boundaries at ~90 Ma, when data from Sif Island (yellow star) indicate offset along Pine Island Rift. Convergence along the Antarctic Peninsula is shown in pink and spreading centres are shown in red, with the locations of margins based on Eagles *et al.* (2004) and Zundel *et al.* (2019b). We have added the thick red line, highlighting divergence along Pine Island Rift. Crustal blocks are marked by different colours. The striped, green area around Sif Island indicates the area between the crustal block boundaries of Jordan *et al.* (2020) and those of Spiegel *et al.* (2016); our data suggest that this area belongs to the Thurston Island block. CI = Chatham Islands.

with and bordering the Chon Aike silicic large igneous province.

The emplacement age and isotopic composition of the Sif Island granite show similarities with rocks in the Thurston Island/Antarctic Peninsula crustal blocks, suggesting that it belongs to this province (Fig. 11). This places the boundary between the Thurston Island and Marie Byrd Land crustal blocks either beneath or along the eastern shear margin (e.g. MacGregor *et al.* 2012) of Thwaites Glacier, similar to what has previously been proposed by Spiegel *et al.* (2016) and Zundel *et al.* (2019b; Fig. 1). In contrast, placing this boundary along Pine Island Rift (e.g. Gohl *et al.* 2007, Jordan *et al.* 2020, Riley *et al.* 2023) would incorrectly include Sif Island in the Marie Byrd Land crustal block. Sif Island represents the south-western-most extent of exposed coastal rocks of Early-Middle Jurassic age, which probably extend beneath Pine Island Glacier (Simões Pereira *et al.* 2020), as well as the south-western-most exposure of Jurassic arc-related rocks.

Conclusions

Ice-front retreat in an area of slow-flowing ice between Thwaites and Pine Island glaciers has revealed the new Sif Island. Sampling of the recently exposed rock from a promontory extending from the island has allowed characterization of its geology and thermal history, as well as providing constraint on its exposure history. Sif Island contains the only subaerial bedrock outcrop between Thwaites and Pine Island glaciers, enabling new inferences to be made regarding the geological and tectonic development of the bedrock underlying the 'weak underbelly' of the WAIS. The geochemical composition and age of the granite constituting Sif Island reveal similarities with Jurassic rocks in the Antarctic Peninsula and Thurston Island crustal blocks. This sets the south-western-most limit of intrusive Jurassic arc-related rocks in West Antarctica, placing the boundary between the Thurston Island and Marie Byrd Land crustal blocks under Thwaites Glacier or at its eastern shear margin.

In addition, the new data reveal that Sif Island has a different thermal history from islands on the northern side of Pine Island Bay, providing the first clear geological evidence that Pine Island Rift was active in the Late Cretaceous. Relative vertical motion along this fault probably exceeded 1 km. Since this time, the Sif Island granite has remained within ~1–2 km of the modern land surface. Cosmogenic nuclide data are consistent with Sif Island either having been buried by an average of ~350 m of ice for millions of years or exposed at the surface for only a few hundred years during the Pleistocene or Holocene. However, other scenarios between these 'end-members' are more plausible.

Future outlook

As the ice extent and grounding zones around Antarctica are likely to continue to retreat over the coming decades and centuries, more islands previously covered by ice will be exposed. This effect will be compounded by isostatic rebound of the lithosphere due to ice-sheet mass loss;

https://doi.org/10.1017/S0954102023000287 Published online by Cambridge University Press

the rate of uplift in the Amundsen Sea sector is currently estimated to be in the region of a few millimetres per year (Whitehouse *et al.* 2019) and locally can reach up to 41 mm/year (Barletta *et al.* 2018). This uplift could lead to significant increases in the area of exposed rock over centennial and millennial timescales, compounded by local sea-level fall due to reduced gravitational pull upon ocean water by the waning ice sheet. In Pine Island Bay, the bed underlying the slow-flowing sector between Thwaites and Pine Island glaciers is predicted to have other areas above or close to sea level (Morlighem *et al.* 2020), which may be revealed as the ice front retreats inland. Whilst providing new opportunities to study the geological history of Antarctica, the retreat of ice grounded on such topographic pinning points will have major implications for grounding-zone stability and thus global sea-level rise.

Acknowledgements

We thank the NBP20-02 science party, support staff and crew of the RV/IB *Nathaniel B. Palmer*, who made it possible to circumnavigate and sample Sif Island, and particularly First Officer Peter Kaple for spotting the island.

This work is from the THOR project, a component of the International Thwaites Glacier Collaboration (ITGC). The cruise was made possible by support from the Natural Environment Research Council (NERC; grant NE/S006664/1 to Claus-Dieter Hillenbrand) and National Science Foundation (NSF; grant 1738942 to Julia Wellner). Ryan Venturelli (grant 2317097), Christine Siddoway and Stuart Thomson (grants 1917176 and 1917009) were supported by the NSF and Keir Nichols and Dylan H. Rood by the NERC (grant NE/S006753/1). Jim W. Marschalek and Tina van de Flierdt acknowledge funding by the additional SSCP NERC DTP and NERC grants NE/R018219/1 and NE/W000172/1. We thank Liam Holder (Imperial College), Barry Coles (Imperial College), Katharina Kreissig (Imperial College) and Mark Evans (BAS) for technical support. We also thank Mark Pecha and the Arizona LaserChron Center staff for help with the zircon U-Pb and Hf isotope analysis; Nicky Giesler (Arizona LaserChron Center) for acquiring the CL imagery; and Peter Reiners, Uttam Chowdhury and the staff at the Arizona Radiogenic Helium Dating Laboratory for assistance with the (U-Th)/He analyses. We are also very grateful to Will Brownscombe at the Natural History Museum (London) for conducting the SEM analyses and calculating the model mineralogy. We also thank Klaus Wilcken and the staff of the Centre for Accelerator Science (CAS) at ANSTO for support during cosmogenic isotope analyses. Discussion with Robert Larter (BAS) helped shape discussion of the tectonic implications of the data. Logistics were provided by NSF-US Antarctic Program and NERC-British Antarctic Survey. ITGC Contribution No. ITGC-100.

We thank Joaquin Bastias and an anonymous reviewer for their constructive feedback on the manuscript.

Author contributions

J.W. Marschalek measured the Nd and Sr isotope compositions and collated and interpreted all of the data with guidance from T. van de Flierdt and C.-D. Hillenbrand. S.N. Thomson and C. Siddoway collected and helped interpret the thermochronological (fission track and (U-Th)/He) data, as well as U-Pb zircon data and zircon Hf isotope data. S.N. Thomson and J.W. Marschalek performed the inverse thermal history modelling. P. Vermeesch, A. Carter, J.W. Marschalek, S.N. Thomson and C. Siddoway measured the U-Pb zircon data. K. Nichols, R.A. Venturelli and D.H. Rood provided and interpreted the cosmogenic nuclide surface exposure data. Major and trace element data were measured by S.J. Hammond. C.-D. Hillenbrand and J. Wellner assisted with collection of the rock samples and circumnavigation of the island during cruise NBP20-02. All authors contributed to writing the text.

Competing interests

The authors declare none.

Supplemental material

A supplemental table will be found at https://doi.org/10.1017/S0954102023000287.

References

Ackert, R.P., Barclay, D.J., Borns, H.W., Calkin, P.E., Kurz, M.D., Fastook, J.L. & Steig, E.J. 1999. Measurements of past ice sheet elevations in interior West Antarctica. *Science*, **286**, 276–280.

Ault, A.K., Gautheron, C. & King, G.E. 2019. Innovations in (U–Th)/He, fission track, and trapped charge thermochronometry with applications to earthquakes, weathering, surface–mantle connections, and the growth and decay of mountains. *Tectonics*, **38**, 10.1029/2018TC005312.

Adams, C.J., Seward, D. & Weaver, S.D. 1995. Geochronology of Cretaceous granites and metasedimentary basement on Edward VII Peninsula, Marie Byrd Land, West Antarctica. *Antarctic Science*, **7**, 265–276.

Amelin, Y. & Davis, W.J. 2005. Geochemical test for branching decay of ^{176}Lu. *Geochimica et Cosmochimica Acta*, **69**, 465–473.

Balco, G. 2017. Production rate calculations for cosmic-ray-muon-produced ^{10}Be and ^{26}Al benchmarked against geological calibration data. *Quaternary Geochronology*, **39**, 150–173.

Balco, G., Stone, J.O., Lifton, N.A. & Dunai, T.J. 2008. A complete and easily accessible means of calculating surface exposure ages or erosion rates from ^{10}Be and ^{26}Al measurements. *Quaternary Geochronology*, **3**, 10.1016/j.quageo.2007.12.001.

Balco, G., Brown, N., Nichols, K., Venturelli, R.A., Adams, J., Braddock, S., *et al.* 2023. Reversible ice sheet thinning in the

Amundsen Sea Embayment during the Late Holocene. *The Cryosphere*, **17**, 10.5194/tc-17-1787-2023.

Barletta, V.R., Bevis, M., Smith, B.E., Wilson, T., Brown, A., Bordoni, A., *et al*. 2018. Observed rapid bedrock uplift in Amundsen Sea Embayment promotes ice-sheet stability. *Science*, **360**, 1335–1339.

Bastias, J., Spikings, R., Riley, T., Ulianov, A., Grunow, A., Chiaradia, M., *et al*. 2021. A revised interpretation of the Chon Aike magmatic province: active margin origin and implications for the opening of the Weddell Sea. *Lithos*, **386**, 106013.

Bastias, J., Spikings, R., Ulianov, A., Riley, T., Burton-Johnson, A., Chiaradia, M., *et al*. 2020. The Gondwanan margin in West Antarctica: insights from Late Triassic magmatism of the Antarctic Peninsula. *Gondwana Research*, **81**, 1–20.

Behrendt, J.C. 2013. The aeromagnetic method as a tool to identify Cenozoic magmatism in the West Antarctic Rift System beneath the West Antarctic Ice Sheet - a review; Thiel subglacial volcano as possible source of the ash layer in the WAISCORE. *Tectonophysics*, **585**, 10.1016/j.tecto.2012.06.035.

Bernet, M. 2009. A field-based estimate of the zircon fission-track closure temperature. *Chemical Geology*, **259**, 10.1016/j.chemgeo.2008.10.043.

Borchers, B., Marrero, S., Balco, G., Caffee, M., Goehring, B., Lifton, N., *et al*. 2016. Geological calibration of spallation production rates in the CRONUS-Earth project. *Quaternary Geochronology*, **31**, 10.1016/j.quageo.2015.01.009.

Cecil, M.R., Gehrels, G., Ducea, M.N. & Patchett, P.J. 2011. U-Pb-Hf characterization of the central Coast Mountains batholith: implications for petrogenesis and crustal architecture. *Lithosphere*, **3**, 247–260.

Corbett, L.B., Bierman, P.R. & Rood, D.H. 2016. An approach for optimizing in situ cosmogenic ^{10}Be sample preparation. *Quaternary Geochronology*, **33**, 24–34.

Cox, S.C., Smith Lyttle, B. & the GeoMAP Team. 2019. *SCAR GeoMAP dataset*. GNS Science, Lower Hutt, New Zealand. Release v.201907. Retrieved from https://doi.org/10.21420/7SH7-6K05

Craddock, J.P., Schmitz, M.D., Crowley, J.L., Larocque, J., Pankhurst, R.J., Juda, N., *et al*. 2017. Precise U-Pb zircon ages and geochemistry of Jurassic granites, Ellsworth-Whitmore terrane, central Antarctica. *GSA Bulletin*, **129**, 118–136.

Diehl, T.M., Holt, J.W., Blankenship, D.D., Young, D.A., Jordan, T.A. & Ferraccioli, F. 2008. First airborne gravity results over the Thwaites Glacier catchment, West Antarctica. *Geochemistry, Geophysics, Geosystems*, **9**, 10.1029/2007GC001878.

Donelick, R.A., O'Sullivan, P.B. & Ketcham, R.A. 2005. Apatite fission-track analysis. *Reviews in Mineralogy and Geochemistry*, **58**, 49–94.

Dunham, C.K., O'Donnell, J.P., Stuart, G.W., Brisbourne, A.M., Rost, S., Jordan, T.A., *et al*. 2020. A joint inversion of receiver function and Rayleigh wave phase velocity dispersion data to estimate crustal structure in West Antarctica. *Geophysical Journal International*, **223**, 1644–1657.

Dziadek, R., Ferraccioli, F. & Gohl, K. 2021. High geothermal heat flow beneath Thwaites Glacier in West Antarctica inferred from aeromagnetic data. *Nature Communications Earth & Environment*, **2**, 1–6.

Eagles, G., Gohl, K. & Larter, R.D. 2004. High-resolution animated tectonic reconstruction of the South Pacific and West Antarctic Margin. *Geochemistry, Geophysics, Geosystems*, **5**, 97–109.

Fanning, C.M. & Laudon, T.S. 1997. Mesozoic volcanism and sedimentation in eastern Ellsworth Land, West Antarctica; conflicting evidence for arc migration? *Geological Society of America, Abstracts with Program*, **29**, A51517.

Fanning, C.M. & Laudon, T.S. 1999. Mesozoic volcanism, plutonism and sedimentation in eastern Ellsworth Land, West Antarctica. Presented at *Eighth International Symposium of Antarctic Earth Sciences*, Wellington, New Zealand, 4–8 July (Abstract). Wellington: The Royal Society of New Zealand.

Fernandez, R.A., Anderson, J.B., Wellner, J.S., Totten, R.L., Hallet, B. & Smith, R.T. 2016. Latitudinal variation in glacial erosion rates from Patagonia and the Antarctic Peninsula (46° S–65° S). *GSA Bulletin*, **128**, 1000–1023.

Flowerdew, M.J., Millar, I.L., Vaughan, A.P.M., Horstwood, M.S.A. & Fanning, C.M. 2006. The source of granitic gneisses and migmatites in the Antarctic Peninsula: a combined U-Pb SHRIMP and laser ablation Hf isotope study of complex zircons. *Contributions to Mineralogy and Petrology*, **151**, 751–768.

Galbraith, R.F. 2005. *Statistics for fission track analysis*. Boca Raton, FL: Chapman & Hall/CRC, 219 pp.

Galbraith, R.F. & Laslett, G.M. 1993. Statistical models for mixed fission track ages. *Nuclear Tracks*, **21**, 459–470.

Gallagher, K. 2012. Transdimensional inverse thermal history modeling for quantitative thermochronology. *Journal of Geophysical Research*, **117**, 10.1029/2011JB008825.

Gehrels, G.E., Valencia, V.A. & Ruiz, J. 2008. Enhanced precision, accuracy, efficiency, and spatial resolution of U-Pb ages by laser ablation-multicollector-inductively coupled plasma-mass spectrometry. *Geochemistry, Geophysics, Geosystems*, **9**, 10.1029/2007GC001805.

Gerrish, L., Fretwell, P. & Cooper, P. 2022. High resolution vector polylines of the Antarctic coastline (7.5) [Dataset]. UK Polar Data Centre, Natural Environment Research Council, UK Research & Innovation. Retrieved from https://doi.org/10.5285/bc71347d-298a-4df3-88b0-cb9a908db166

Gleadow, A.J.W. 1981. Fission-track dating methods: what are the real alternatives? *Nuclear Tracks*, **5**, 3–14.

Gleadow, A.J.W., Hurford, A.J. & Quaife, R.D. 1976. Fission track dating of zircon: improved etching techniques. *Earth and Planetary Science Letters*, **33**, 273–276.

Goehring, B.M., Wilson, J. & Nichols, K. 2019. A fully automated system for the extraction of *in situ* cosmogenic carbon-14 in the Tulane University cosmogenic nuclide laboratory. *Nuclear Instruments and Methods in Physics Research Section B: Beam Interactions with Materials and Atoms*, **455**, 284–292.

Gohl, K. 2012. Basement control on past ice sheet dynamics in the Amundsen Sea Embayment, West Antarctica. *Palaeogeography, Palaeoclimatology, Palaeoecology*, **335**, 35–41.

Gohl, K., Denk, A., Eagles, G. & Wobbe, F. 2013. Deciphering tectonic phases of the Amundsen Sea Embayment shelf, West Antarctica, from a magnetic anomaly grid. *Tectonophysics*, **585**, 113–123.

Gohl, K., Teterin, D., Eagles, G., Netzeband, G., Grobys, J. & Parsiegla, N. 2007. Geophysical survey reveals tectonic structures in the Amundsen Sea embayment, West Antarctica. *US Geological Survey Open-File Report*, 2007-1047. Retrieved from http://pubs.usgs.gov/of/2007/1047/srp/srp047/

Graham, A.G., Wåhlin, A., Hogan, K.A., Nitsche, F.O., Heywood, K.J., Totten, R.L., *et al*. 2022. Rapid retreat of Thwaites Glacier in the pre-satellite era. *Nature Geoscience*, **15**, 706–713.

Griffin, W.L. 2008. *GLITTER*: data reduction software for laser ablation ICP-MS. *In* Sylvestor, P., *ed.*, *Laser ablation ICP-MS in the Earth sciences: current practices and outstanding issues*. Quebec: Mineralogical Association of Canada, 308–311.

Guenthner, W.R., Reiners, P.W. & Chowdhury, U. 2016. Isotope dilution analysis of Ca and Zr in apatite and zircon (U-Th)/He chronometry. *Geochemistry, Geophysics, Geosystems*, **17**, 10.1002/2016GC006311.

Guenthner, W.R., Reiners, P.W., Ketcham, R.A., Nasdala, L. & Giester, G. 2013. Helium diffusion in natural zircon: radiation damage, anisotropy, and the interpretation of zircon (U-Th)/He thermochronology. *American Journal of Science*, **313**, 145–198.

Hansen, K., Stevens, J. & Shuman, C. 2022. Ice lost, island dound? *NASA Earth Observatory*. Retrieved from https://www.earthobservatory.nasa.gov/images/149755/ice-lost-island-found

https://doi.org/10.1017/S0954102023000287 Published online by Cambridge University Press

Haran, T., Bohlander, J., Scambos, T., Painter, T. & Fahnestock, M. 2014. MODIS Mosaic of Antarctica 2008–2009 (MOA2009) image map. Boulder, CO: National Snow and Ice Data Center. Retrieved from https://nsidc.org/data/nsidc-0593/versions/2

Hippe, K. & Lifton, N.A. 2014. Calculating isotope ratios and nuclide concentrations for *in situ* cosmogenic ^{14}C analyses. *Radiocarbon*, **56**, 1167–1174.

Hogan, K.A., Larter, R.D., Graham, A.G., Arthern, R., Kirkham, J.D., Totten Minzoni, R., *et al*. 2020. Revealing the former bed of Thwaites Glacier using sea-floor bathymetry: implications for warm-water routing and bed controls on ice flow and buttressing. *The Cryosphere*, **14**, 2883–2908.

Hourigan, J.K., Reiners, P.W. & Brandon, M.T. 2005. U-Th zonation-dependent alpha-ejection in (U-Th)/He chronometry. *Geochimica et Cosmochimica Acta*, **69**, 10.1016/j.gea.2005.01.024.

Hurford, A.J. 1990. Standardization of fission track dating calibration: recommended by the Fission Track Working Group of the I.U.G.S. *Subcommission on Geochronology. Chemical Geology*, **80**, 171–178.

Hurford, A.J. & Green, P.F. 1983. The zeta-age calibration of fission-track dating. *Isotope Geoscience*, **1**, 285–317.

Jackson, S.E., Pearson, N.J., Griffin, W.L. & Belousova, E.A. 2004. The application of laser ablation-inductively coupled plasma-mass spectrometry to in situ U-Pb zircon geochronology. *Chemical Geology*, **211**, 47–69.

Jacobsen, S.B. & Wasserburg, G.J. 1980. Sm-Nd isotopic evolution of chondrites. *Earth and Planetary Science Letters*, **50**, 139–155.

Jordan, T.A., Riley, T.R. & Siddoway, C.S. 2020. The geological history and evolution of West Antarctica. *Nature Reviews Earth & Environment*, **1**, 117–133.

Jordan, T.A., Ferraccioli, F., Vaughan, D.G., Holt, J.W., Corr, H., Blankenship, D.D. & Diehl, T.M. 2010. Aerogravity evidence for major crustal thinning under the Pine Island Glacier region (West Antarctica). *GSA Bulletin*, **122**, 714–726.

Kalberg, T., Gohl, K., Eagles, G. & Spiegel, C. 2015. Rift processes and crustal structure of the Amundsen Sea Embayment, West Antarctica, from 3D potential field modelling. *Marine Geophysical Research*, **36**, 10.1007/s11001-015-9261-0.

Ketcham, R.A., Gautheron, C. & Tassan-Got, L. 2011. Accounting for long alpha-particle stopping distances in (U-Th-Sm)/He geochronology: refinement of the baseline case. *Geochimica et Cosmochimica Acta*, **75**, 10.1016/j.gca.2011.10.011.

Ketcham, R.A., Carter, A., Donelick, R.A., Barbarand, J. & Hurford, A.J. 2007. Improved modeling of fission-track annealing in apatite. *American Mineralogist*, **92**, 799–810.

Kipf, A., Mortimer, N., Werner, R., Gohl, K., Van Den Bogaard, P., Hauff, F. & Hoernle, K. 2012. Granitoids and dykes of the Pine Island Bay region, West Antarctica. *Antarctic Science*, **24**, 473–484.

Klages, J.P., Salzmann, U., Bickert, T., Hillenbrand, C.-D., Gohl, K., Kuhn, G., *et al*. 2020. Temperate rainforests near the South Pole during peak Cretaceous warmth. *Nature*, **580**, 81–86.

Larter, R.D., Cunningham, A.P., Barker, P.F., Gohl, K. & Nitsche, F.O. 2002. Tectonic evolution of the Pacific margin of Antarctica 1. Late Cretaceous tectonic reconstructions. *Journal of Geophysical Research - Solid Earth*, **107**, EPM-5.

Lifton, N., Sato, T. & Dunai, T.J. 2014. Scaling in situ cosmogenic nuclide production rates using analytical approximations to atmospheric cosmic-ray fluxes. *Earth Planetary Science Letters*, **386**, 10.1016/j.epsl.2013.10.052.

Lindow, J., Kamp, P.J., Mukasa, S.B., Kleber, M., Lisker, F., Gohl, K., *et al*. 2016. Exhumation history along the eastern Amundsen Sea coast, West Antarctica, revealed by low-temperature thermochronology. *Tectonics*, **35**, 2239–2257.

Lisker, F. & Olesch, M. 1998. Cooling and denudation history of western Marie Byrd Land, Antarctica, based on apatite fission-tracks. In Haute, P. & Corte, F., eds, *Advances in fission-track geochronology*. Dordrecht: Springer, 225–240.

MacGregor, J., Catania, G., Markowski, M. & Andrews, A. 2012. Widespread rifting and retreat of ice-shelf margins in the eastern Amundsen Sea Embayment between 1972 and 2011. *Journal of Glaciology*, **58**, 10.3189/2012JoG11J262.

McCarron, J.J. & Larter, R.D. 1998. Late Cretaceous to early Tertiary subduction history of the Antarctic Peninsula. *Journal of the Geological Society*, **155**, 255–268.

McDonough, W.F. & Sun, S.S. 1995. The composition of the Earth. *Chemical Geology*, **120**, 10.1016/0009-2541(94)00140-4.

McFadden, R.R., Teyssier, C., Siddoway, C.S., Cosca, M.A. & Fanning, C.M. 2015. Mid-Cretaceous oblique rifting of West Antarctica: emplacement and rapid cooling of the Fosdick Mountains migmatite-cored gneiss dome. *Lithos*, **232**, 306–318.

McFadden, R.R., Teyssier, C., Siddoway, C.S., Whitney, D.L. & Fanning, C.M. 2010. Oblique dilation, melt transfer, and gneiss dome emplacement. *Geology*, **38**, 375–378.

Mehling, A. 2015. *Hornblende-Plagioklas Thermobarometrie an Graniten der Backer Inseln in der Pine Island Bay, Westantarktis*. Bachelor thesis. Bremen: University of Bremen.

Millan, R., Rignot, E., Bernier, V., Morlighem, M. & Dutrieux, P. 2017. Bathymetry of the Amundsen Sea Embayment sector of West Antarctica from Operation IceBridge gravity and other data. *Geophysical Research Letters*, **44**, 1360–1368.

Millar, I.L., Willan, R.C.R., Wareham, C.D. & Boyce, A.J. 2001. The role of crustal and mantle sources in the genesis of granitoids of the Antarctic Peninsula and adjacent crustal blocks. *Journal of the Geological Society*, **158**, 855–867.

Morlighem, M., Rignot, E., Binder, T., Blankenship, D., Drews, R., Eagles, G., *et al*. 2020. Deep glacial troughs and stabilizing ridges unveiled beneath the margins of the Antarctic ice sheet. *Nature Geoscience*, **13**, 132–137.

Mouginot, J., Rignot, E. & Scheuchl, B. 2019. Continent-wide, interferometric SAR phase-mapping of Antarctic ice velocity. *Geophysical Research Letters*, **46**, 10.1029/2019GL083826.

Mukasa, S.B. & Dalziel, I.W. 2000. Marie Byrd Land, West Antarctica: evolution of Gondwana's Pacific margin constrained by zircon U-Pb geochronology and feldspar common-Pb isotopic compositions. *Geological Society of America Bulletin*, **112**, 611–627.

Müller, R.D., Gohl, K., Cande, S.C., Goncharov, A. & Golynsky, A.V. 2007. Eocene to Miocene geometry of the West Antarctic rift system. *Australian Journal of Earth Sciences*, **54**, 1033–1045.

Murray, K.E., Orme, D.A. & Reiners, P.W. 2014. Effects of U-Th-rich grain boundary phases on apatite helium ages. *Chemical Geology*, **390**, 135–151.

Muto, A., Anandakrishnan, S., Alley, R.B., Horgan, H.J., Parizek, B.R., Koellner, S., *et al*. 2019. Relating bed character and subglacial morphology using seismic data from Thwaites Glacier, West Antarctica. *Earth and Planetary Science Letters*, **507**, 199–206.

Nelson, D.A. & Cottle, J.M. 2018. The secular development of accretionary orogens: linking the Gondwana magmatic arc record of West Antarctica, Australia and South America. *Gondwana Research*, **63**, 15–33.

Nichols, K.A. & Goehring, B.M. 2019. Isolation of quartz for cosmogenic *in situ* ^{14}C analysis. *Geochronology*, **1**, 43–52.

Nichols, K.A., Rood, D.H., Venturelli, R.A., Balco, G., Adams, J.R., Guillaume, L., *et al*. 2023. Offshore-onshore record of Last Glacial Maximum-to-present grounding line retreat at Pine Island Glacier, Antarctica, *Geology*, 10.1130/G51326.1.

Pankhurst, R.J. & Rapela, C.R. 1995. Production of Jurassic rhyolite by anatexis of the lower crust of Patagonia. *Earth and Planetary Science Letters*, **134**, 23–36.

Pankhurst, R.J., Millar, I.L., Grunow, A.M. & Storey, B.C. 1993. The pre-Cenozoic magmatic history of the Thurston Island crustal block, West Antarctica. *Journal of Geophysical Research - Solid Earth*, **98**, 11835–11849.

Pankhurst, R.J., Riley, T.R., Fanning, C.M. & Kelley, S.P. 2000. Episodic silicic volcanism in Patagonia and the Antarctic Peninsula:

https://doi.org/10.1017/S0954102023000287 Published online by Cambridge University Press

chronology of magmatism associated with the break-up of Gondwana. *Journal of Petrology*, **41**, 605–625.

Pankhurst, R.J., Weaver, S.D., Bradshaw, J.D., Storey, B.C. & Ireland, T.R. 1998. Geochronology and geochemistry of pre-Jurassic superterranes in Marie Byrd Land, Antarctica. *Journal of Geophysical Research - Solid Earth*, **103**, 2529–2547.

Patchett, P.J. 1983. Importance of the Lu-Hf isotopic system in studies of planetary chronology and chemical evolution. *Geochimica and Cosmochimica Acta*, **47**, 81–91.

Patchett, P.J. & Tatsumoto, M. 1980. A routine high-precision method for Lu-Hf isotope geochemistry and chronology. *Contributions to Mineralogy and Petrology*, **75**, 263–267.

Pearce, N.J., Perkins, W.T., Westgate, J.A., Gorton, M.P., Jackson, S.E., Neal, C.R. & Chenery, S.P. 1997. A compilation of new and published major and trace element data for NIST SRM 610 and NIST SRM 612 glass reference materials. *Geostandards Newsletter*, **21**, 115–144.

Intergovernmental Panel on Climate Change. 2019. *IPCC special report on the ocean and cryosphere in a changing climate* (Pörtner, H.-O., Roberts, D.C., Masson-Delmotte, V., Zhai, P., Tignor, M., Poloczanska, E., *et al*., *eds*). Cambridge: Cambridge University Press, 755 pp.

Rahn, M., Wang, H. & Dunkl, I. 2019. A natural long-term annealing experiment for the zircon fission track system in the Songpan-Garzê flysch, China. *Terra Nova*, **31**, 10.1016/j.lithos.2015.06.023.

Reiners, P.W. & Brandon, M.T. 2006. Using thermochronology to understand orogenic erosion. *Annual Review of Earth and Planetary Science*, **34**, 10.1146/annurev.earth.34.031405.125202

Richard, S.M., Smith, C.H., Kimbrough, D.L., Fitzgerald, P.G., Luyendyk, B.P. & McWilliams, M.O. 1994. Cooling history of the northern Ford Ranges, Marie Byrd Land, West Antarctica. *Tectonics*, **13**, 837–857.

Riefstahl, F., Gohl, K., Davy, B., Hoernle, K., Mortimer, N., Timm, C., *et al*. 2020. Cretaceous intracontinental rifting at the southern Chatham Rise margin and initialisation of seafloor spreading between Zealandia and Antarctica. *Tectonophysics*, **776**, 228298.

Rignot, E., Mouginot, J., Morlighem, M., Seroussi, H. & Scheuchl, B. 2014. Widespread, rapid grounding line retreat of Pine Island, Thwaites, Smith, and Kohler glaciers, West Antarctica, from 1992 to 2011. *Geophysical Research Letters*, **41**, 3502–3509.

Rignot, E., Mouginot, J., Scheuchl, B., Van Den Broeke, M., Van Wessem, M.J. & Morlighem, M. 2019. Four decades of Antarctic Ice Sheet mass balance from 1979–2017. *Proceedings of the National Academy of Sciences of the United States of America*, **116**, 1095–1103.

Riley, T.R., Leat, P.T., Pankhurst, R.J. & Harris, C. 2001. Origins of large volume rhyolitic volcanism in the Antarctic Peninsula and Patagonia by crustal melting. *Journal of Petrology*, **42**, 1043–1065.

Riley, T.R., Flowerdew, M.J., Pankhurst, R.J., Leat, P.T., Millar, I.L., Fanning, C.M. & Whitehouse, M.J. 2017. A revised geochronology of Thurston Island, West Antarctica, and correlations along the proto-Pacific margin of Gondwana. *Antarctic Science*, **29**, 47–60.

Riley, T.R., Millar, I.L., Carter, A., Flowerdew, M.J., Burton-Johnson, A., Bastias, J., *et al*. 2023. Evolution of an accretionary complex (LeMay Group) and terrane translation in the Antarctic Peninsula. *Tectonics*, **42**, e2022TC007578.

Scambos, T.A., Bell, R.E., Alley, R.B., Anandakrishnan, S., Bromwich, D.H., Brunt, K., *et al*. 2017. How much, how fast?: A science review and outlook for research on the instability of Antarctica's Thwaites Glacier in the 21st century. *Global and Planetary Change*, **153**, 16–34.

Scarrow, J.H., Pankhurst, R.J., Leat, P.T. & Vaughan, A.P. 1996. Antarctic Peninsula granitoid petrogenesis: a case study from Mount Charity, north-eastern Palmer Land. *Antarctic Science*, **8**, 193–206.

Scherer, E., Münker, C. & Mezger, K. 2001. Calibration of the lutetium-hafnium clock. *Science*, **293**, 683–687.

Schroeder, D.M., Blankenship, D.D., Young, D.A., Witus, A.E. & Anderson, J.B. 2014. Airborne radar sounding evidence for deformable sediments and outcropping bedrock beneath Thwaites Glacier, West Antarctica. *Geophysical Research Letters*, **41**, 7200–7208.

Siddoway, C.S., Baldwin, S.L., Fitzgerald, P.G., Fanning, C.M. & Luyendyk, B.P. 2004. Ross Sea mylonites and the timing of intracontinental extension within the West Antarctic Rift System. *Geology*, **32**, 57–60.

Simões Pereira, P., van de Flierdt, T., Hemming, S.R., Frederichs, T., Hammond, S.J., Brachfeld, S., *et al*. 2020. The geochemical and mineralogical fingerprint of West Antarctica's weak underbelly: Pine Island and Thwaites glaciers. *Chemical Geology*, **550**, 119649.

Simões Pereira, P., van de Flierdt, T., Hemming, S.R., Hammond, S.J., Kuhn, G., Brachfeld, S., *et al*. 2018. Geochemical fingerprints of glacially eroded bedrock from West Antarctica: detrital thermochronology, radiogenic isotope systematics and trace element geochemistry in Late Holocene glacial-marine sediments. *Earth-Science Reviews*, **182**, 204–232.

Sláma, J., Košler, J., Condon, D.J., Crowley, J.L., Gerdes, A., Hanchar, J.M., *et al*. 2008. Plešovice zircon - a new natural reference material for U-Pb and Hf isotopic microanalysis. *Chemical Geology*, **249**, 1–35.

Smith, A.M., Jordan, T.A., Ferraccioli, F. & Bingham, R.G. 2013. Influence of subglacial conditions on ice stream dynamics: seismic and potential field data from Pine Island Glacier, West Antarctica. *Journal of Geophysical Research - Solid Earth*, **118**, 1471–1482.

Söderlund, U., Patchett, P.J., Vervoort, J.D. & Isachsen, C.E. 2004. The ^{176}Lu decay constant determined by Lu-Hf and U-Pb isotope systematics of Precambrian mafic intrusions. *Earth and Planetary Science Letters*, **219**, 311–324.

Spiegel, C., Lindow, J., Kamp, P.J., Meisel, O., Mukasa, S., Lisker, F., *et al*. 2016. Tectonomorphic evolution of Marie Byrd Land - implications for Cenozoic rifting activity and onset of West Antarctic glaciation. *Global and Planetary Change*, **145**, 98–115.

Storey, B.C., Brown, R.W., Carter, A., Doubleday, P.A., Hurford, A.J., Macdonald, D.I.M. & Nell, P.A.R. 1996. Fission-track evidence for the thermotectonic evolution of a Mesozoic–Cenozoic fore-arc, Antarctica. *Journal of the Geological Society*, **153**, 65–82.

Tanaka, T., Togashi, S., Kamioka, H., Amakawa, H., Kagami, H., Hamamoto, T., *et al*. 2000. JNdi-1: a neodymium isotopic reference in consistency with LaJolla neodymium. *Chemical Geology*, **168**, 10.1016/S0009-2541(00)00198-4.

Tulloch, A.J., Mortimer, N., Ireland, T.R., Waight, T.E., Maas, R., Palin, J.M., *et al*. 2019. Reconnaissance basement geology and tectonics of south Zealandia. *Tectonics*, **38**, 516–551.

Twinn, G., Riley, T., Fox, M. & Carter, A. 2022. Thermal history of the southern Antarctic Peninsula during Cenozoic oblique subduction. *Journal of the Geological Society*, **179**, jgs2022-008.

van Wyk de Vries, M., Bingham, R.G. & Hein, A.S. 2017. A new volcanic province: an inventory of subglacial volcanoes in West Antarctica. *Special Publication of the Geological Society of London*, No. **461**, 231–248.

Vermeesch, P. 2018. *IsoplotR*: a free and open toolbox for geochronology. *Geoscience Frontiers*, **9**, 1479–1493.

Vermeesch, P. 2021. On the treatment of discordant detrital zircon U-Pb data. *Geochronology*, **3**, 247–257.

Vermeesch, P. & Tian, Y. 2014. Thermal history modelling: *HeFTy vs. QTQt*. *Earth Science Reviews*, **139**, 10.1016/j.earscirev.2014. 09.010.

Vervoort, J.D., Patchett, P.J., Söderlund, U. & Baker, M. 2004. The isotopic composition of Yb and the precise and accurate determination of Lu concentrations and Lu/Hf ratios by isotope dilution using MC-ICPMS. *Geochemistry, Geophysics, Geosystems*, **5**, 10.1029/2004GC000721.

Wareham, C.D., Millar, I.L. & Vaughan, A.P. 1997. The generation of sodic granite magmas, western Palmer Land, Antarctic Peninsula. *Contributions to Mineralogy and Petrology*, **128**, 81–96.

Weis, D., Kieffer, B., Maerschalk, C., Barling, J., De Jong, J., Williams, G.A., *et al*. 2006. High-precision isotopic characterization of USGS reference materials by TIMS and MC-ICP-MS. *Geochemistry, Geophysics, Geosystems*, **7**, 10.1029/2006GC001283.

Wever, H.E., Millar, I.L. & Pankhurst, R.J. 1994. Geochronology and radiogenic isotope geology of Mesozoic rocks from eastern Palmer Land, Antarctic Peninsula: crustal anatexis in arc-related granitoid genesis. *Journal of South American Earth Sciences*, **7**, 69–83.

Whitehouse, P.L., Gomez, N., King, M.A. & Wiens, D.A. 2019. Solid Earth change and the evolution of the Antarctic ice sheet. *Nature Communications*, **10**, 1–14.

Wilch, T.I., McIntosh, W.C. & Panter, K.S. 2021. Chapter 5.4a Marie Byrd Land & Ellsworth Land I. Volcanology. In Smellie, J.L., Panter, K.S. & Geyer, A., eds, *Volcanism in Antarctica:* 200 *million years of subduction, rifting and continental break-up*. Geological Society, London, Memoir **55**, 10.1144/M55-2019-39.

Wilcken, K.M., Codilean, A.T., Fülöp, R.H., Kotevski, S., Rood, A.H., Rood, D.H., *et al*. 2022. Accelerator mass spectrometry of ^{10}Be and ^{26}Al at low nuclide concentrations. *Geochronology*, **4**, 339–352.

Woodhead, J., Hergt, J., Shelley, M., Eggins, S. & Kemp, R. 2004. Zircon Hf-isotope analysis with an excimer laser, depth profiling, ablation of complex geometries, and concomitant age estimation. *Chemical Geology*, **209**, 121–135.

Yamada, R., Murakami, M. & Tagami, T. 2007. Statistical modelling of annealing kinetics of fission tracks in zircon; reassessment of laboratory experiments. *Chemical Geology*, **236**, 75–91.

Ziaja, W. & Ostafin, K. 2019. Origin and location of new Arctic islands and straits due to glacial recession. *Ambio*, **48**, 25–34.

Zundel, M., Spiegel, C., Lisker, F. & Monien, P. 2019a. Post Mid-Cretaceous tectonic and topographic evolution of Western Marie Byrd Land, West Antarctica: insights from apatite fission track and (U-Th-Sm)/He data. *Geochemistry Geophysics Geosystems*, **20**, 5831–5848.

Zundel, M., Spiegel, C., Mehling, A., Lisker, F., Hillenbrand, C.D., Monien, P. & Klügel, A. 2019b. Thurston Island (West Antarctica) between Gondwana subduction and continental separation: a multistage evolution revealed by apatite thermochronology. *Tectonics*, **38**, 878–897.

https://doi.org/10.1017/S0954102023000287 Published online by Cambridge University Press